

Article

# Bubble Wrap-like Carbon-Coated Rattle-Type silica@silicon Nanoparticles as Hybrid Anode Materials for Lithium-Ion Batteries via Surface-Protected Etching

Angelica Martino <sup>1</sup>, Jiyun Jeon <sup>2</sup>, Hyun-Ho Park <sup>1</sup>, Hochun Lee <sup>2</sup> and Chang-Seop Lee <sup>1,\*</sup>

<sup>1</sup> Department of Chemistry, Keimyung University, Daegu 42601, Republic of Korea; angelicamartino97@kmu.kr (A.M.); rubchem@kmu.ac.kr (H.-H.P.)

<sup>2</sup> Department of Energy Science and Engineering, Daegu Gyeongbuk Institute of Science & Technology (DGIST), Daegu 42988, Republic of Korea; jiyunn1234@dgist.ac.kr (J.J.); dukelee@dgist.ac.kr (H.L.)

\* Correspondence: surfkm@kmu.ac.kr; Tel.: +82-53-580-5192

**Abstract:** Severe volumetric expansion (~400%) limits practical application of silicon nanoparticles as anode materials for next-generation lithium-ion batteries (LIBs). Here, we describe the fabrication and characterization of a conformal polydopamine carbon shell encapsulating rattle-type silica@silicon nanoparticles (PDA-PEI@PVP-SiO<sub>2</sub>@Si) with a tunable void structure using a dual template strategy with TEOS and (3-aminopropyl)triethoxysilane (APTES) pretreated with polyvinylpyrrolidone (PVP K30) as SiO<sub>2</sub> sacrificial template via a modified Stöber process. Polyethylene imine (PEI) crosslinking facilitated the construction of an interconnected three-dimensional bubble wrap-like carbon matrix structure through hydrothermal treatment, pyrolysis, and subsequent surface-protected etching. The composite anode material delivered satisfactory capacities of 539 mAh g<sup>-1</sup> after 100 cycles at 0.1 A g<sup>-1</sup>, 512.76 mAh g<sup>-1</sup> after 200 cycles at 1 A g<sup>-1</sup>, and 453 mAh g<sup>-1</sup> rate performance at 5 A g<sup>-1</sup>, respectively. The electrochemical performance of PDA-PEI@PVP-SiO<sub>2</sub>@Si was attributed to the rattle-type structure providing void space for Si volume expansion, PVP K30-pretreated APTES/TEOS SiO<sub>2</sub> seeds via catalyst-free, hydrothermal-assisted Stöber protecting Si/C spheres upon etching, carbon coating strategy increasing Si conductivity while stabilizing the solid electrolyte interface (SEI), and PEI carbon crosslinks providing continuous conductive pathways across the electrode structure. The present work describes a promising strategy to synthesize tunable yolk shell C@void@Si composite anode materials for high power/energy-density LIBs applications.

**Keywords:** lithium-ion battery; silicon anode; carbon nanomaterials; silica coating; yolk shell structure; surface protected etching; template method; polydopamine coating



**Citation:** Martino, A.; Jeon, J.; Park, H.-H.; Lee, H.; Lee, C.-S. Bubble Wrap-like Carbon-Coated Rattle-Type silica@silicon Nanoparticles as Hybrid Anode Materials for Lithium-Ion Batteries via Surface-Protected Etching. *Batteries* **2024**, *10*, 53. <https://doi.org/10.3390/batteries10020053>

Academic Editor: Torsten Brezesinski

Received: 28 November 2023

Revised: 24 January 2024

Accepted: 24 January 2024

Published: 1 February 2024



**Copyright:** © 2024 by the authors. Licensee MDPI, Basel, Switzerland. This article is an open access article distributed under the terms and conditions of the Creative Commons Attribution (CC BY) license (<https://creativecommons.org/licenses/by/4.0/>).

## 1. Introduction

Elevated levels of greenhouse gases, particularly carbon dioxide, have led to global environmental challenges, resulting in climate change with adverse effects on biodiversity and human survival [1]. To address these issues, international agreements like the Paris Agreement [2] and organizations such as the United Nations (UN) and European Union (EU) have implemented strategic measures to regulate and facilitate the transition from a fossil fuel-dependent economy to a carbon-neutral one, aiming to mitigate climate change [3,4]. Despite these efforts, as of 2022, 91% of energy generation still relies on fossil fuels, and CO<sub>2</sub> emissions from the transportation sector increased to around 8 Gt CO<sub>2</sub>, a 3% rise from the 2021 levels. Global environmental policies are now concentrated on promoting low- and zero-emission vehicle operations and intensifying efforts toward transportation decarbonization, aiming to achieve the Net Zero Emission (NZE) scenario in the transportation sector by 2050 [5]. Major economies are increasingly adopting lithium-ion battery (LIB) technology for the electrification of road vehicles, with electric vehicles (EV) gaining momentum since 2022. However, a noticeable material scarcity arises from the

growing disparity between the supply and demand for critical materials in these advanced applications [6].

LIB technology has emerged as the predominant power source for numerous commercial electronic devices due to its simplified cell chemistry [7,8]. Furthermore, the LIB system exhibits a broad operating voltage range, minimal self-discharge, and limited memory defects, necessitating low maintenance [9]. Despite the commendable structural stability of current graphite anodes with a gravimetric capacity of only  $372 \text{ mAh g}^{-1}$  in commercial LIB, they are deemed inadequate for high-energy/energy density applications, such as in electric vehicles (EVs) or grid-scale operations [10]. Identifying new battery materials that are capable of delivering not only high energy density but also features like rapid charging [11], extended driving range on a single charge [12], cost-effectiveness with minimal critical metal usage (e.g., nickel (Ni) and lithium (Li)) [13], robust stability in extreme temperatures [14], and overall prolonged battery life is imperative for battery manufacturers in material selection. Meeting these stringent criteria is essential for the successful transition to pure electric or hybrid electric vehicles [7–14].

Given the imperative need for enhanced specific capacity in advanced electric vehicle (EV) applications, considerable research has focused on employing silicon (Si) as a viable alternative to graphite in current lithium-ion battery (LIB) technology. Silicon offers a notable advantage with an outstanding theoretical capacity of  $4200 \text{ mAh g}^{-1}$  for  $\text{Li}_{22}\text{Si}_5$ . Importantly, Si operates at a moderate onset voltage potential of 0.3–0.4 V above  $\text{Li}/\text{Li}^+$ , effectively minimizing undesirable side reactions such as Li plating [15–17]. As the second most abundant element in the Earth's crust, coupled with its environmental friendliness, Si as an active anode material holds significant promise for powering EVs, contributing to lower production costs and enhanced market value [18,19]. Beyond its cost-effectiveness and high theoretical capacity to improve driving range, Si exhibits fast charging capabilities and stable cycling performance, particularly in extremely low-temperature conditions, making it highly attractive for future LIB applications [20].

In pristine conditions, Si exhibits repetitive volumetric expansion, leading to the formation of a mechanically unstable solid electrolyte interface (SEI) layer. The continual expansion and contraction of Si morphology result in the increased exposure of bare Si particles, rendering them susceptible to electrolyte decomposition. This process excessively consumes finite  $\text{Li}^+$  ions and results in the formation of a thicker SEI film, ultimately degrading reversible capacity and desiccating the entire cell [21,22]. Additionally, challenges such as Si's inferior electronic conductivity ( $\text{Si} \approx 10^{-3} \text{ S cm}^{-1}$ ) compared to graphite and activated carbons ( $\text{C} \approx 1 \text{ S cm}^{-1}$ ), severe Si particle aggregation due to high surface energy, and the presence of a native oxide layer in as-received Si contribute to dispersion stability issues. These challenges often lead to an uneven distribution of active materials within the anode structure, causing particle isolation, crack formation, and pulverization during extended lithiation/delithiation cycles [23].

Diverse Si morphologies, including nanoparticles [24,25], nanowires [26], nanotubes [27], nanospheres [28], nanoporous structures [29], and 3D microstructures [30], have been investigated, and various techniques have been developed to enhance the electrochemical performance of Si. Notably, our research group has integrated a range of carbon nanomaterials, such as carbon nanofibers [31,32], carbon nanotubes [33,34], graphene [35,36], and graphene quantum dots [34,37], to augment the electronic conductivity of Si. This approach provides protection against parasitic electrolyte decomposition reactions and mitigates detrimental volume changes. Despite the promise of highly functional carbon nanomaterials, challenges such as high-temperature thermal processing [38], expensive precursor materials [39,40], low material yield [41], and complex synthetic routes involving multiple organic reactions and purifications at intermediate steps [42,43] persist as obstacles to electric vehicle (EV) applications. Addressing the urgent need for cost-effective and efficient synthetic routes to produce lithium-ion batteries (LIBs) with advanced features for EVs is crucial, emphasizing the optimization of Si's advantages while addressing issues of severe volume expansion and low conductivity [24–43].

Si-based anodes typically face two primary limitations for practical use in advanced applications: (1) inevitable volumetric fluctuations leading to SEI-related mechanical failure and (2) intrinsically low electronic conductivity causing sluggish charge transfer kinetics. To address these challenges, a straightforward strategy involves incorporating a hollow, void space between Si and the carbon coating layer. This void space acts as a buffer, accommodating the volume changes of Si nanoparticles during cycling without causing severe structural damage to the protective carbon shell. Previous studies on Si anodes employing a yolk shell structure have demonstrated notable enhancements in electrochemical cycling stability. Specifically, Si/SiO<sub>x</sub> hybrids [44] and yolk shell-structured Si@void@C nanocomposite anodes [45] exhibited significant improvements in stability and electrochemical performance, attributed to the additional void space capable of accommodating internal volume changes in Si [44,45].

Numerous studies have extensively documented the encapsulation of silicon (Si) nanoparticles within an outer carbon shell, showcasing advantages such as enhanced structural integrity and electronic conductivity for Si. The carbon coating strategy involves a diverse range of coating precursors, with polydopamine (PDA) standing out as a long-utilized material due to its capability to form conformal coatings on individual Si nanoparticles through solution-phase coating [45]. Additionally, polyethylene imines (PEI), known for their highly positive charges and versatile structures compatible with various substrates, serve as effective functional coatings. The combination of PEI with polyvinyl alcohol (PVA) through in situ thermal polymerization results in a deformable polymer binder with a cross-linked network, exhibiting strong binding for Si [46]. The co-polymerization of PDA and PEI as a coating material has been reported to enhance hydrophilicity and chemical stability for various substrates [47]. Drawing on these findings, employing PDA and PEI as a protective layer emerges as a viable strategy for encapsulating Si nanoparticles [45–47].

Silica (SiO<sub>2</sub>) hard templates, typically synthesized via the Stöber route [48], represent a widely employed approach for constructing yolk shell structures. The synthesis of SiO<sub>2</sub> via this method involves the hydrolysis and condensation reactions of silicon alkoxides (e.g., tetraethyl orthosilicate (TEOS)) in an alcohol solvent (e.g., ethyl alcohol (EtOH)), facilitated by water and a base catalyst (e.g., ammonia) [49]. Achieving a yolk shell structure requires the removal of the SiO<sub>2</sub> patterning substrate, which can be accomplished through either a reactive ion etching (RIE) process [50] or a chemical removal method employing solution-phase chemical etching. Common etchants include strong acids, such as 45–48% hydrofluoric acid (HF) or its diluted form as in buffered HF (BHF), sometimes combined with inorganic fluorides like sodium fluoride (NaF) and ammonium fluoride (NH<sub>4</sub>F) in a buffered oxide etch (BOE) [51,52]. Alternatively, high concentrations of a strong base, such as sodium hydroxide (NaOH) at boiling temperatures, can be utilized for template removal [53].

Despite the simplicity of the SiO<sub>2</sub> coating process via the Stöber route, challenges arise in the utilization of SiO<sub>2</sub> hard templates, and there are safety concerns associated with handling highly corrosive and toxic hydrofluoric acid (HF) during template removal. First, achieving tunability in the HF-assisted chemical etching of SiO<sub>2</sub> proves difficult due to high etching rates, even at dilute concentrations (1000 Å min<sup>-1</sup> in a 10:1 buffered HF solution) [54]. Second, utilizing TEOS as a SiO<sub>2</sub> precursor results in a continuous, dense, and rigid SiO<sub>2</sub> coating on Si, making it susceptible to mechanical stress during cycling [55]. Additionally, using TEOS alone poses disadvantages such as sluggish hydrolysis and condensation kinetics, the requirement for base catalysis, limited control over particle size and morphology, monodispersity issues, and potential toxicity concerns. Third, though surface-protected etching has shown improvement in SiO<sub>2</sub> shell tunability through poly(vinylpyrrolidone) (PVP) K15 coating [56], it involves a complex synthetic process with multiple refluxing steps, making it tedious [57]. Therefore, employing a longer PVP K30 chain in a simplified one-pot technique offers a promising alternative strategy to enhance

polymer chain stability, preventing the total dissolution of Si active materials and structural damage in yolk shell Si/C composites [57].

This study presents a three-pronged fabrication strategy aimed at overcoming the aforementioned limitations of Si. The proposed synthetic process involves the integration of rattle-type SiO<sub>2</sub>@Si nanoparticles, coated with PDA and cross-linked with PEI polymers. These nanoparticles are derived from TEOS and APTES precursors. Preceding this, a hydrothermally assisted Stöber process is employed, followed by pyrolysis and surface-protected NaOH etching. The rationale for employing these methods is threefold. First, the yolk shell structure allows for void spaces, enabling core Si nanoparticles to expand without causing structural damage to the carbon protective shell. Second, the PDA coating and PEI-derived polymer network act as a protective barrier for Si nanoparticles, concurrently enhancing their conductivity. Lastly, PVP K30 molecules embedded within the APTES/TEOS–SiO<sub>2</sub> shells contribute to maintaining the structural integrity of the carbon coating during template removal.

To investigate the impact of a yolk shell structure on electrochemical performance, a composite material was synthesized using the same process but with a core shell configuration. These hybrid composites served as anode materials for LIBs, and their electrochemical performances were assessed under diverse cycling conditions. The representative yolk shell composite material (PDA–PEI@PVP–SiO<sub>2</sub>@Si) exhibited an initial capacity of 719 mAh g<sup>−1</sup>, maintaining 539 mAh g<sup>−1</sup> after 100 cycles at 0.1 A g<sup>−1</sup>. Under a higher current density of 5 A g<sup>−1</sup>, it sustained a capacity of 453 mAh g<sup>−1</sup>, surpassing the performance of core shell composite counterparts. The notable electrochemical performance of the PDA–PEI@PVP–SiO<sub>2</sub>@Si composite was attributed to the synergistic effects of the three-pronged fabrication strategy employed in this study.

## 2. Materials and Methods

### 2.1. Materials and Reagents

Reagents employed in this study were of analytical grade. They were used as obtained without further purification. Sulfuric acid (H<sub>2</sub>SO<sub>4</sub>, 98.0%), hydrogen peroxide (H<sub>2</sub>O<sub>2</sub>, 30.0%), and PVP K30 were obtained from Daejung Chemical & Metals (Siheung, Republic of Korea). Si nanoparticles (powder, APS ≤ 50 nm, 98.0%) were purchased from Alfa Aesar (Haverhill, MA, USA). TEOS (≥99.0%), dopamine hydrochloride for PDA coating (C<sub>8</sub>H<sub>12</sub>ClNO<sub>2</sub>), and PEI solution (MW~750,000; 50 wt.% in H<sub>2</sub>O) were purchased from Sigma-Aldrich (St. Louis, MO, USA). APTES (≥99.0%) was purchased from AcroSeal™, Thermo Scientific Chemicals (Loughborough, UK). EtOH (C<sub>2</sub>H<sub>5</sub>OH, 94.5%) was purchased from Samchun Pure Chemical Co., Ltd. (Seoul, Republic of Korea). NaOH was supplied by Duksan Pure Chemicals (Ansan, Republic of Korea). High-purity industrial argon (Ar, 99.0%) gas used for pyrolysis was supplied by PSG Corp, Busan, Republic of Korea. All aqueous solutions were prepared and washed with deionized (DI) water.

### 2.2. Fabrication of Yolk Shell and Core Shell PDA–PEI@PVP–SiO<sub>2</sub>@Si Composites

Figure 1 depicts the one-pot hydrothermal synthesis of yolk shell composite materials through the Stöber process. The process involves enhancing the hydrophilicity of Si nanoparticles via a piranha solution pre-treatment, generating abundant surface –OH groups (Si–OH) [37].

Piranha-treated Si–OH (0.5 g) underwent dispersion in EtOH (480 mL) mixed with DI (120 mL) through 2 h sonication. Following cooling, TEOS (7 mL) and APTES (2 mL) were successively added to the dispersed Si–OH solution at a controlled rate (~0.5 mL min<sup>−1</sup>) under rigorous stirring (300 rpm) to prevent aggregation. PVP K30 (0.5 g), dissolved in DI (10 mL), was introduced, and the solution was mechanically stirred overnight at room temperature to ensure the completion of hydrolysis and condensation reactions. Subsequently, a PDA (0.5 g) and PEI solution (2.5 mL) was successively incorporated, and the solution was stirred overnight until a viscous solution was observed. To facilitate PVP K30 loading into SiO<sub>2</sub> shells and enhance PDA–PEI carbon coating, the resulting

solution was transferred to a Teflon-lined container and reacted at 140 °C for 24 h. After hydrothermal treatment, products were collected via filtration, washed extensively with EtOH and DI, followed by overnight drying in a vacuum oven at 80 °C. The carbonization of polymer coatings was accomplished via pyrolysis in a tube furnace at 800 °C for 5 h in an Ar atmosphere.

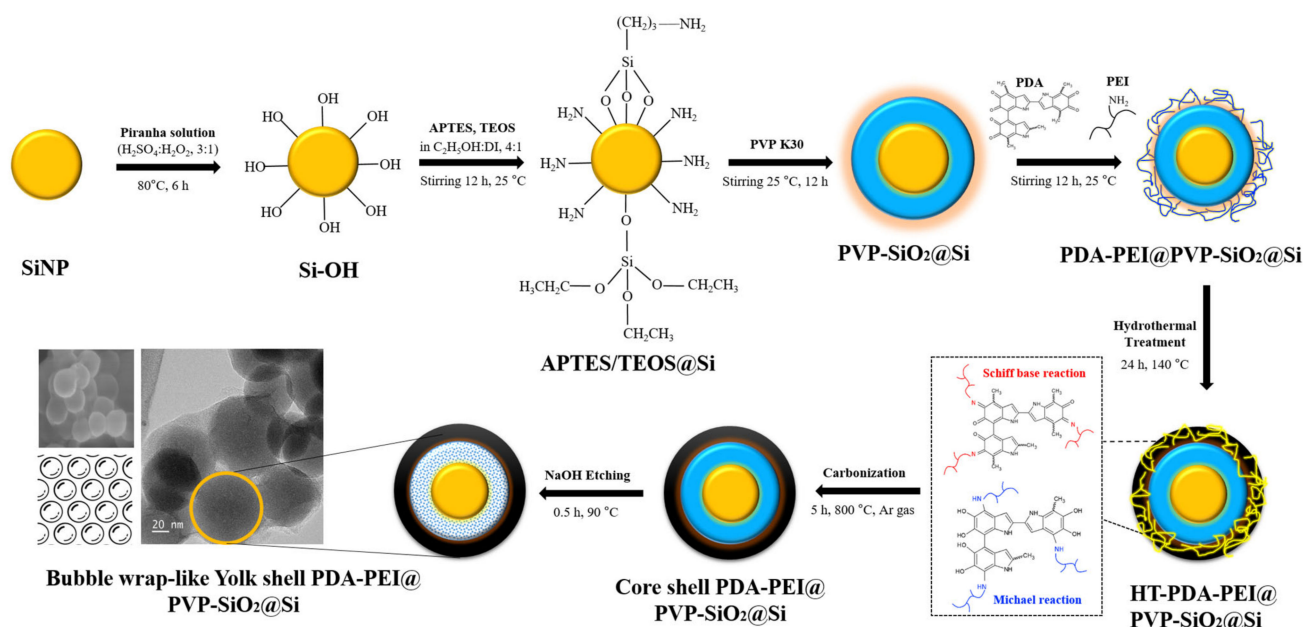


**Figure 1.** Schematic representation of the fabrication process of core shell and yolk shell PDA-PEI@PVP-SiO<sub>2</sub>@Si composites.

Following pyrolysis, the core shell PDA-PEI@PVP-SiO<sub>2</sub>@Si composite was collected. Simultaneously, the representative yolk shell PDA-PEI@PVP-SiO<sub>2</sub>@Si composite was obtained through an additional chemical etching process using 2.5 M NaOH at 90 °C, followed by DI washing. A black powder was collected after overnight oven drying at 80 °C. To investigate the impact of APTES in SiO<sub>2</sub> synthesis, yolk shell and core shell composites with solely TEOS-derived SiO<sub>2</sub> shells were alternately fabricated (PDA-PEI@TEOS@Si). Additionally, a PEI-free composite (PDA@PVP-SiO<sub>2</sub>@Si) was synthesized to assess PDA-PEI coating efficiency. The effect of surface-protected etching was examined by fabricating SiO<sub>2</sub> shells without PVP K30 (PDA-PEI@SiO<sub>2</sub>@Si). Finally, the impact of hydrothermal treatment (HT-PDA-PEI@PVP-SiO<sub>2</sub>@Si) on composite fabrication was compared to composites obtained through the traditional Stöber process and through carbon coating performed at room temperature (RT-PDA-PEI@PVP-SiO<sub>2</sub>@Si).

### 2.3. Materials Characterization

Structural and morphological characteristics of fabricated composites were examined with a field-emission scanning electron microscope (FE-SEM, S-4800, Hitachi, Tokyo, Japan) at 100 kV. A high-resolution transmission electron microscope provided insights to internal yolk shell structures (TEM, JEM-2100, JEOL, Tokyo, Japan). Energy-dispersive X-ray (EDS, ARL-3460, Thermo Fisher Scientific, Waltham, MA, USA) mapping was used to perform qualitative and quantitative microanalyses of elements in sample composites. Crystalline compositions were characterized using powder X-ray diffraction (XRD) measurements with Cu-K $\alpha$  radiation ( $K = 1.5418 \text{ \AA}$ ) at  $2\theta = 2\text{--}90^\circ$  in a 2 kW Ultima IV (Rigaku, Tokyo, Japan) instrument. Raman spectra were obtained within 500–3000 cm<sup>-1</sup> wavelength using a Jobin Yvon LabRAM HR-800 (Horiba, Kyoto, Japan) with laser light irradiation ( $\lambda = 514 \text{ nm}$ ). Fourier-transform infrared spectroscopy (FTIR) analysis was conducted within a frequency range of 400–4000 cm<sup>-1</sup> using potassium bromide (KBr) pellets on a Nicolet 6700 spectrophotometer (Thermo Fisher Scientific, Waltham, MA, USA). Al-K $\alpha$

twin-anode X-ray photoelectron spectroscopy (XPS, Multilab-2000, Thermo Fisher Scientific, Waltham, MA, USA) was used to evaluate chemical bonding states in composite materials. Mass loadings of Si, SiO<sub>x</sub>, and carbonaceous materials present in composite samples were extrapolated from thermogravimetric analysis (TGA) coupled with differential thermal analysis (DTA). Derivative thermogravimetric (DTG) curves in percent mass loss per degree Celsius were collected using a Diamond TG/DTA system (PerkinElmer, Waltham, MA, USA) from 20–900 °C at a heating rate of 10 °C min<sup>-1</sup> in a nitrogen-protected environment to prevent rapid oxidation of Si into SiO<sub>2</sub>. BET (Brunauer–Emmett–Teller) analysis was conducted in a QuadraSorb SI ©2000-16 (Quantachrome Instruments, Boynton Beach, FL, USA) to calculate the specific surface area and determine porous character of samples using the Barette-Joyner-Halenda (BJH) model from the adsorption branch of the isotherm. Before measurements, the studied samples were degassed under vacuum for 24 h at 60 °C. Additional physical characterization were performed to the cycled composites after 200 cycles at 1 A g<sup>-1</sup> via FE-SEM focused on surface view of the electrodes.

#### 2.4. Electrochemical Testing

The fabricated yolk shell and core shell composites were used as active anode materials in a two-electrode battery system. To evaluate electrochemical performance of the resultant composite material, a conventional slurry mixture was obtained by mechanically mixing 80 wt.% of the active composite material with 10 wt.% of binder and 10 wt.% of Super P as a conductive agent casted on a copper (Cu) foil as the current collector. Circular disks with a diameter of 14 mm were punched from the electrode plate with an average load density of ~1 mg cm<sup>-2</sup> to obtain working electrodes from fabricated core shell and yolk shell composites. Depending on the coating efficiency of the slurry mixture onto the electrode plate after vacuum drying at 80 °C for 24 h, carboxymethyl cellulose (CMC) binder in DI water solvent and polyvinylidene fluoride (PVDF) dissolved in N-Methyl-2-pyrrolidone (NMP) organic solvent were employed as the binder materials during slurry preparation.

Coin-type cells (2032) were assembled inside an Ar-filled glove box using working electrodes from fabricated composites, a metal Li foil as the counter/reference electrode, and a standard polyethylene membrane (Celgard 2600, Polypore Korea, Ltd., Cheonan, Republic of Korea) as the separator soaked in the electrolyte. The electrolyte employed was 1.0 M of LiPF<sub>6</sub> in 3:7 *w/w* ethylene carbonate (EC)/ethyl methyl carbonate (EMC) with 7 wt.% of fluorethylene carbonate (FEC) to increase solvation and improve cycling stability. Cycling voltammetry (CV) was conducted at a scan rate of 0.1 mV s<sup>-1</sup> with voltages of 0.01–1.5 V at 25 °C. Electrochemical impedance spectroscopy (EIS) measurements were conducted at frequencies of 100 kHz to 10 mHz and amplitude of 5 mV on a Chi 660F electrochemical analysis instrument (CH Instruments, Inc. Shanghai, China). Cycling tests, high-rate loading tests, and galvanostatic charge/discharge profile measurements were executed using a battery tester (Neware Co., Ltd., Shenzhen, China) at voltages of 0.01–1.5V (vs. Li/Li<sup>+</sup>). Cycling performance tests at a high-current density of 1 A g<sup>-1</sup> over 200 extended cycles were also performed. The specific capacity was computed based on the mass loading of the anode material in working electrode disks.

### 3. Results and Discussion

#### 3.1. Role of APTES in the Synthesis of SiO<sub>2</sub>@Si Shells

SEM images of TEOS- and APTES/TEOS-derived SiO<sub>2</sub> shells precursors are shown in Figure 2.

The FE-SEM image and FT-IR spectra of Si following piranha pre-treatment are illustrated in Figure S1 (Supplementary Materials). Figure 2a displays a non-uniform, thick coating of TEOS-derived SiO<sub>2</sub> shell on Si, while Figure 2b exhibits a more uniform SiO<sub>2</sub> coating with reduced Si–OH nanoparticle agglomeration in the APTES/TEOS-derived SiO<sub>2</sub>. Notably, a conformal spherical morphology with an average particle diameter of ~60 nm was observed, attributed to APTES's self-catalytic activity in sol-gel SiO<sub>2</sub> particle formation,

fostering siloxane bond formation with abundant silanol groups on Si–OH, even without the presence of an alkali catalyst [55].

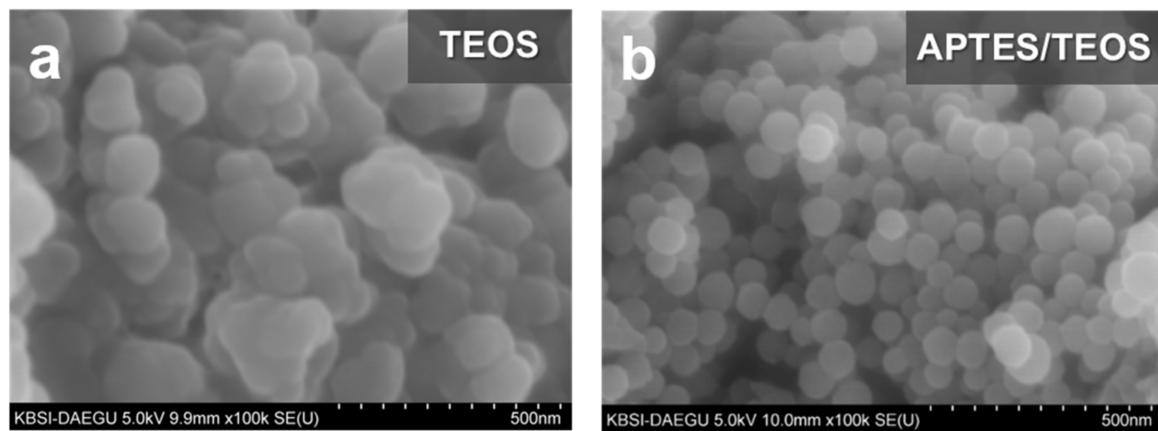


**Figure 2.** FE-SEM images of (a) TEOS-derived SiO<sub>2</sub>@Si and (b) APTES/TEOS-derived SiO<sub>2</sub>@Si via catalyst-free Stöber route synthesis at room temperature (500 nm magnification).

Supporting evidence for APTES’s self-catalyzing role in promoting SiO<sub>2</sub> growth and effective coating on Si–OH is furnished by TEM results, as depicted in Figure 3. Figure 3a exhibits notable particle agglomeration of TEOS–SiO<sub>2</sub>@Si without discernible structural organization. In Figure 3b, an isolated TEOS–SiO<sub>2</sub>@Si particle features a ~50 nm Si nanoparticle enveloped by a thick SiO<sub>2</sub> coating, displaying evident aggregation with dark patches in the background. The in-plane lattice fringe, highlighted in Figure 3c, reveals a 0.3096 nm ordered lattice spacing attributed to the (111) plane of Si [37]. The inset in Figure 3d displays a corresponding fast Fourier transform (FFT) pattern, confirming sustained Si crystallinity following the SiO<sub>2</sub> sol-gel coating process using TEOS.

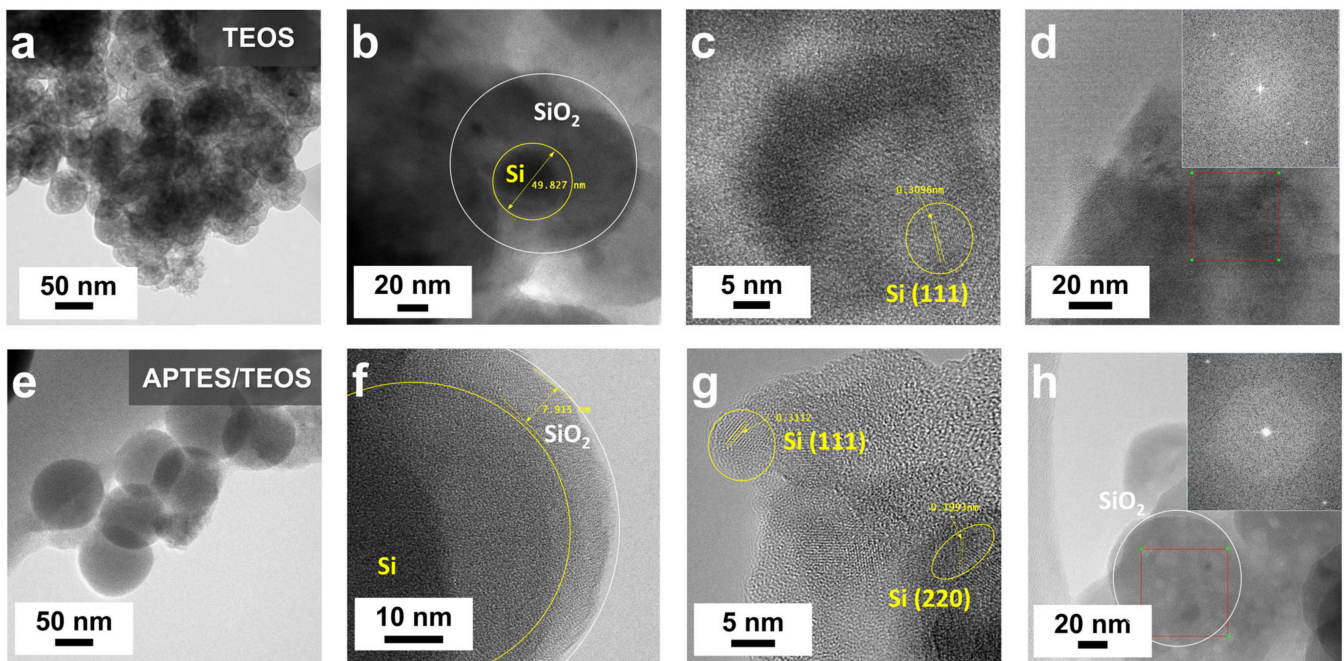


**Figure 3.** TEM images of (a–d) TEOS-derived SiO<sub>2</sub>@Si and (e–h) APTES/TEOS-derived SiO<sub>2</sub>@Si nanoparticles after a catalyst-free, sol-gel synthesis at room temperature. The Si nanoparticles and SiO<sub>2</sub> coating are highlighted as yellow and white circles, respectively.

Figure 3e highlights APTES's role as a structure-directing agent, depicting APTES/TEOS-derived SiO<sub>2</sub>@Si with an absence of visible particle aggregation and a uniform spherical morphology. Figure 3f illustrates an isolated APTES/TEOS-SiO<sub>2</sub>@Si nanoparticle with a thin, conformal SiO<sub>2</sub> coating (~8 nm). Two distinct crystal lattice spacings, observed in Figure 3g (0.3112 nm and 0.1993 nm), align well with the (111) and (220) planes of Si, respectively [31,37]. The inset image in Figure 3h displays notable bright spots, affirming the preserved crystallinity of Si during the SiO<sub>2</sub> sol-gel coating process using APTES.

Prior works on the co-condensation of TEOS and APTES in EtOH and DI have predominantly utilized APTES as a surface modifier in post-modification or grafting scenarios to introduce amino groups to Si [35]. This application extends to APTES serving as a precursor material to SiO<sub>2</sub> [55], often employed in soft-hard template strategies utilizing other surfactants, like cetyl trimethyl ammonium bromide (CTAB) [58]. To illustrate the pivotal function of APTES as a self-catalytic, structure-directing agent in conjunction with TEOS, the hydrolysis and condensation reaction mechanism and the formation of siloxane networks from APTES and TEOS are detailed in Figure S2 (Supplementary Materials).

The choice of APTES and TEOS for synthesizing SiO<sub>2</sub> shells is guided by the unique properties and functionalities introduced by APTES into the SiO<sub>2</sub> matrix. In the conventional Stöber process, TEOS undergoes slow hydrolysis and condensation, necessitating extended reaction times for SiO<sub>2</sub> formation. Additionally, the condensation of TEOS into siloxane networks requires a potent base catalyst. Furthermore, employing TEOS with a base catalyst offers limited control over particle size, growth, and morphology. Factors such as temperature, rotations per minute, and pH level influence reaction conditions. Achieving uniform particle size with TEOS is challenging, as incomplete control over synthesis conditions may yield a broad distribution of particle sizes.

Prior investigations have elucidated the self-catalytic mechanism inherent to APTES. In a co-condensation modification utilizing APTES and TEOS, the Stöber route yielded highly monodispersed, ~60 nm-modified nanosilica particles [59]. The self-catalytic role of APTES was also explored in atomic layer deposition (ALD) for SiO<sub>2</sub> from APTES, water, and ozone gas [60]. Another study employing APTES as the sole SiO<sub>2</sub> precursor in simultaneous condensation copolymerization with ascorbic acid resulted in a crosslinked carbon matrix reinforced by dispersed nano-SiO<sub>2</sub>, further suggesting APTES's self-catalysis into SiO<sub>2</sub> shells after mechanical stirring at 60 °C for 8 h [55]. The intricate reaction mechanism underlying APTES's self-catalytic activity is expounded in Figure S2a (Supplementary Materials).

It is important to highlight that while pristine Si nanoparticles inherently acquire a native oxide layer due to unavoidable surface oxidation during manufacturing, treating them with piranha solution is generally preferred. This treatment optimizes the number of surface hydroxyl groups, facilitating bond formation with the silanol groups of APTES and TEOS. The -OH groups resulting from piranha pre-treatment on Si-OH energetically promote siloxane bond formation in a condensation reaction, leading to a well-ordered silane layer on the Si surface within APTES/TEOS, even in the absence of alkali catalysts.

XPS analysis was conducted to confirm elemental composition changes during SiO<sub>2</sub> synthesis from two precursors and subsequent coating onto Si nanoparticles, as depicted in Figure 4. The survey spectra of SiO<sub>2</sub> shells derived from the two precursors are compared in Figure S3. High-resolution Si 2p spectra of TEOS-derived SiO<sub>2</sub>@Si revealed peaks at 102.71 eV (Si-O-Si), 100.59 eV (Si-OH), and a small peak at 98.86 eV (Si). O 1s scans displayed peaks at 531.98 eV (Si-O-Si) and 530.67 eV (Si-OH). These findings indicated the successful conversion of the majority of TEOS silane precursor into SiO<sub>2</sub>, with trace Si-OH potentially originating from unreacted hydroxyl groups. The presence of a small Si peak suggested inefficient coating, leaving some Si nanoparticles bare. C 1s spectra highlighted different carbon environments within TEOS organic groups. O 1s peaks at 532.59 eV (O-C=O) and 533.99 eV (O-C=O) revealed the distinct bonding environments of O atoms in ester groups [61,62].

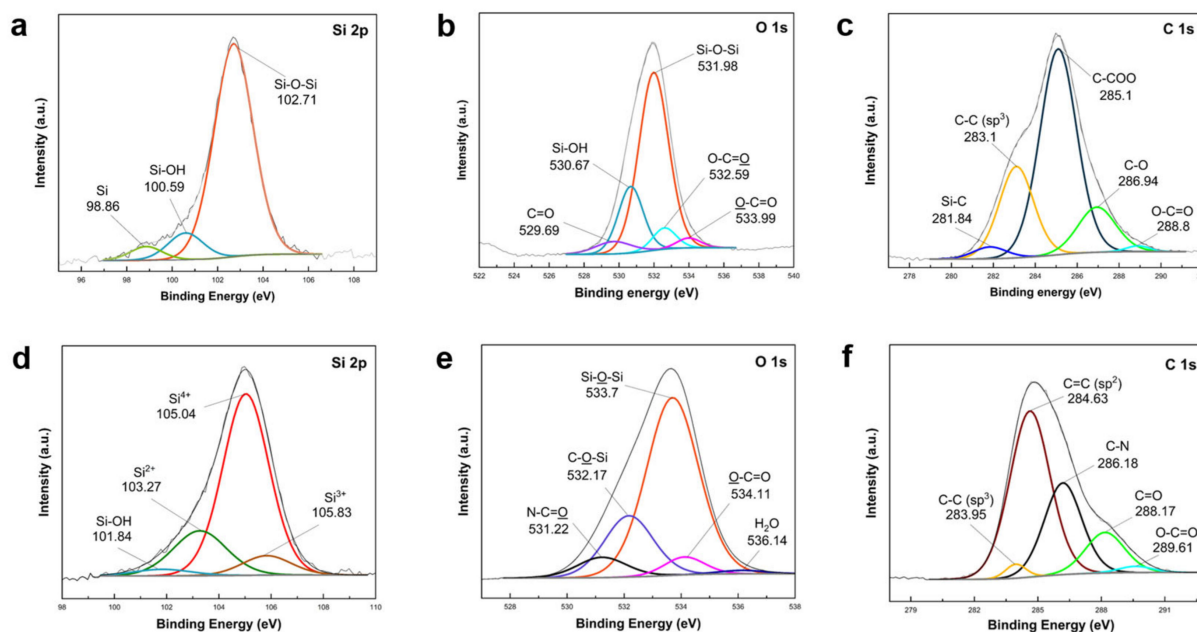


**Figure 4.** XPS high resolution (a,d) Si 2p, (b,e) O 1s, and (c,f) C 1s scans of (a–c) TEOS–SiO<sub>2</sub>@Si and (d–f) APTES/TEOS–SiO<sub>2</sub>@Si samples.

In Si 2p scans of APTES/TEOS-derived SiO<sub>2</sub>@Si nanoparticles (Figure 4d), Si–OH and pure Si peaks were absent, signifying the successful condensation of all Si–OH into a SiO<sub>2</sub> layer. Si 2p scans revealed a relatively high-intensity shift of the Si–O–Si peak to a higher binding energy of 105.04 eV, attributed to a particle charge on the deposited SiO<sub>2</sub> coating. This shift, observed in silicon oxides, differed from non-oxidized species that exhibited no shift [61,63]. The Si 2p peak at 105.04 eV indicated Si in the 4<sup>+</sup> oxidation state, while broad peaks at 103.27 eV and 105.83 eV were assigned to Si<sup>2+</sup> and Si<sup>3+</sup> oxidation states of amorphous SiO<sub>x</sub>, respectively [64]. The small peak of Si–OH at 101.84 eV further supported SiO<sub>2</sub> coating construction. The O 1s peaks (Figure 4e) at 532.17 eV (C–O–Si), 531.22 eV (N–C=O), and 534.11 eV (O–C=O) aligned with C 1s scans (Figure 4f), corroborating successful amino-functionalized SiO<sub>2</sub> modification from APTES [65]. A negligible peak at 536 eV was attributed to trace amounts of adsorbed H<sub>2</sub>O molecules during sample analysis [66]. Furthermore, N 1s peaks at 401.51 eV, ascribing to C–N, confirmed the effective SiO<sub>2</sub> modification into an amino-functionalized SiO<sub>2</sub> coating due to the chemical compositions of APTES [65].

### 3.2. Multifaceted Effects of Proposed Modified Stöber via Hydrothermal Treatment

Ensuring the uniform coating of the Si active material with a thin carbon layer is imperative to create a protective barrier against direct electrolyte contact. Given the anticipated Si volume expansion, effective etching of the SiO<sub>2</sub> sacrificial layer during template removal is essential to facilitate the formation of an internal void space. Additionally, the rigid and amorphous nature of SiO<sub>2</sub> poses specific challenges. The yolk shell structure's void space serves not only to absorb Si volume expansion but also plays a crucial role in averting crack formation on the carbon shell due to repetitive volume fluctuations. Furthermore, the carbon coating must endure the etching process without compromising its mechanical structure. Addressing these conditions necessitates a three-fold strategy involving (1) the creation of robust and uniform SiO<sub>2</sub> shells through APTES/TEOS dual precursor, (2) utilizing PVP K30 polymer for surface protection during etching, adding flexibility to the rigid SiO<sub>2</sub> matrix, and (3) implementing a conformal PDA carbon coating with PEI crosslinking through the proposed hydrothermal treatment. A control sample was fabricated following identical procedures at room temperature.

Opting for PVP K30 polymer over the previously utilized PVP K15 in the existing literature presents several advantages in this study. PVP K30, characterized by a higher molecular weight compared to PVP K15, offers improved properties such as enhanced viscosity, solubility, and the capacity to form more stable complexes with other substances. Typically employed as a stabilizing agent, PVP aids in preventing particle agglomeration and fortifying the stability of particles or in the preparation of polymeric films and coatings. In the current investigation, PVP K30 polymer was specifically chosen to afford surface protection to SiO<sub>2</sub> shells during rigorous etching conditions. The elongated polymer chains resulting from the greater molecular weight of PVP K30, in contrast to PVP K15, were deemed essential to establish a robust protective layer, ensuring the steric stabilization of SiO<sub>2</sub> particles. Moreover, the relatively higher molecular weight of PVP K30 played a critical role in preventing the collapse of the outer carbon coating and selectively etched inner SiO<sub>2</sub> layer, preserving the integrity of the yolk structure.

The reported efficacy and stability enhancement of PDA carbon shells through hydrothermal treatment, even after subjecting them to 40 wt.% HF etching for 2 h, underscores the significance of this approach [67]. Leveraging this concept enables the construction of a robust PDA coating on Si, ensuring satisfactory structural integrity. It is noteworthy that the proposed fabrication process preserves the inherent crystallinity of the Si active material throughout template removal. Si crystallinity validation throughout the entire composite fabrication process was conducted via XRD analysis, with results confirming the maintained crystallinity, as depicted in Figure 5.

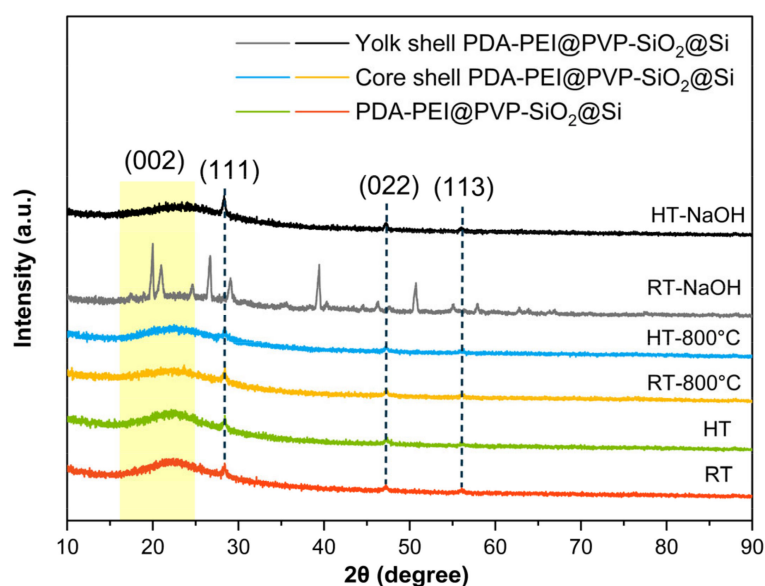


**Figure 5.** XRD patterns of core shell and yolk shell PDA-PEI@PVP-SiO<sub>2</sub>@Si composites fabricated from hydrothermally-assisted modified Stöber (HT) compared with the control group for fabricating the conventional sol-gel reaction at room temperature (RT), before and after pyrolysis, and after NaOH etching processes.

The crystallinity of the Si active material throughout the composite fabrication process was monitored using XRD analysis. XRD patterns for pristine Si nanoparticles, TEOS-SiO<sub>2</sub>@Si, and APTES/TEOS-SiO<sub>2</sub>@Si are presented in Figure S4 for comparison (see Supplementary Materials). As depicted in Figure 5, the Si crystallinity remained well-preserved in both synthetic routes. Alongside a broad peak centered at  $2\theta = 26.0^\circ$ , attributed to the (002) plane of graphitic carbon materials resulting from PDA-PEI carbonization, intense diffraction peaks at  $2\theta = 28.4^\circ$ ,  $47.3^\circ$ , and  $56.1^\circ$  were observed, well-indexed to the (111), (220), and (311) facets of a typical face-centered cubic Si crystal (reference code 98-065-2265, Figure S5). Representative Si peaks persisted in composites, with or without hydrothermal treatment, even after high-temperature pyrolysis. Notably, these peaks dis-

appeared in composite samples without hydrothermal treatment after the etching process. Conversely, composite samples synthesized through the proposed hydrothermal route retained Si peaks post NaOH etching. XRD results corroborated the beneficial impact of hydrothermal treatment on crafting yolk shell composites without compromising Si crystallinity during template removal.

Apart from preserving Si crystallinity during severe etching, hydrothermal treatment demonstrated enhanced coating efficiency in the prepared composites (Figure 6).

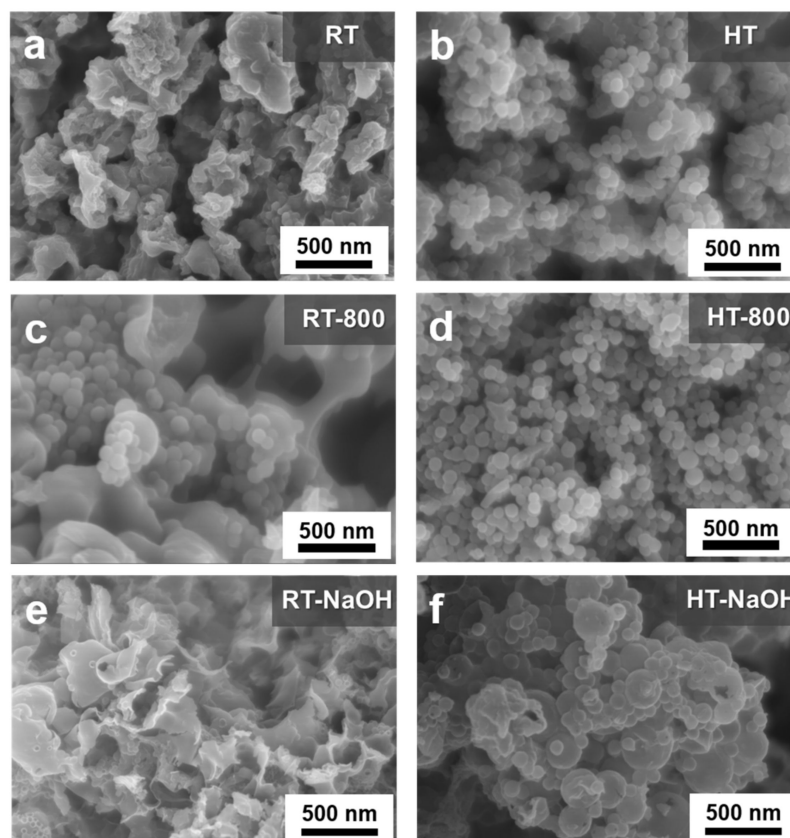


**Figure 6.** FE-SEM images of (a,c,e) composite samples prepared via RT and (b,d,f) HT before and after pyrolysis and NaOH etching of SiO<sub>2</sub> template.

In Figure 6a, a one-pot synthetic route at room temperature reveals a sheet-like structure surrounding aggregated spherical SiO<sub>2</sub>@Si nanoparticles. In contrast, Figure 6b illustrates composites obtained through the hydrothermal treatment Stöber route, displaying a well-dispersed SiO<sub>2</sub> shell uniformly coated with PDA-PEI and reduced aggregation. A substantial contrast in carbon coating efficiency between both routes is evident in the comparison of Figure 6c,d after pyrolysis. Room temperature composite samples exhibit uneven carbon coating, with exposed APTES/TEOS-SiO<sub>2</sub>@Si nanoparticles clustered above sheet-like PDA-PEI carbon structures. Despite PVP-surface protection during NaOH etching, composites without hydrothermal treatment incur severe damage to the carbon network structure (Figure 6e), compromising PDA-PEI carbon coatings and crosslinking structures during SiO<sub>2</sub> template removal. Conversely, composite samples prepared with hydrothermal treatment maintain distinct PDA carbon coatings with minimal structural damage (Figure 6f). TEM images (Figure S6, Supplementary Materials) visually depict the impact of hydrothermal treatment, resulting in a more complete PDA carbon coating and PEI crosslinking to APTES/TEOS-SiO<sub>2</sub>@Si nanoparticles.

### 3.3. Significance of PVP K30 Surface Protection during NaOH Etching

Chemical bonds in composite samples throughout the fabrication process were analyzed to assess direct PVP K30 loading. Successful loading was confirmed via FTIR analysis, as depicted in Figure 7.

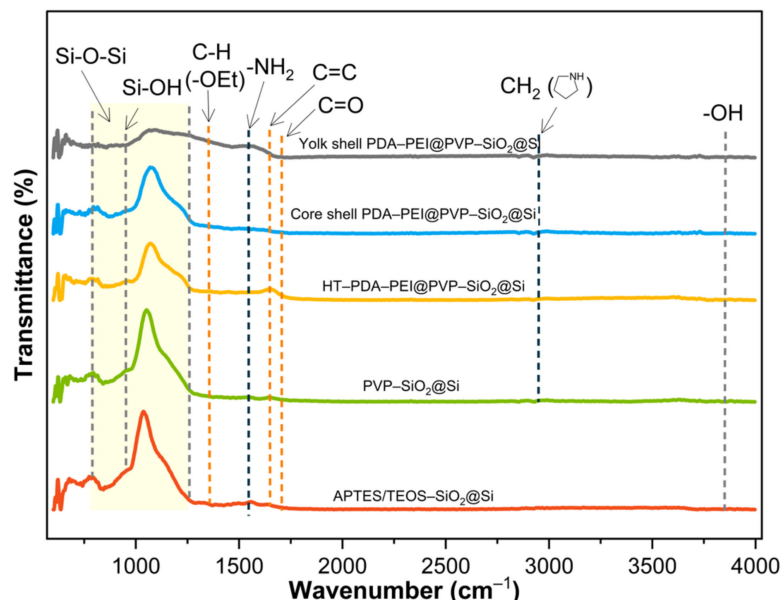


**Figure 7.** FTIR spectra of APTES/TEOS-SiO<sub>2</sub>@Si, PVP-SiO<sub>2</sub>@Si, HT-PDA-PEI@PVP-SiO<sub>2</sub>@Si, core shell PDA-PEI@PVP-SiO<sub>2</sub>@Si, and yolk shell PDA-PEI@PVP-SiO<sub>2</sub>@Si samples with PVP K30-surface protection.

The initial detection of abundant surface -OH groups around  $\sim 3400\text{ cm}^{-1}$ , subsequent to piranha pre-treatment, vanished entirely in the spectra of all samples. This disappearance indicates the successful condensation reactions of APTES/TEOS. The adsorption band at  $1544\text{ cm}^{-1}$ , corresponding to -NH<sub>2</sub> groups from the APTES precursor solution, remained evident. A weak absorption band at  $1348\text{ cm}^{-1}$ , attributed to C-H bending vibrations of unhydrolyzed -OEt groups, was identified in APTES/TEOS-SiO<sub>2</sub>@Si. Its intensity diminished further upon loading PVP K30 to produce PVP-SiO<sub>2</sub>@Si, suggesting hydrogen bond formation with the SiO<sub>2</sub> surface. Additional peaks at  $2925\text{ cm}^{-1}$  (-CH<sub>2</sub> stretching modes in the pyrrolidone ring),  $1703\text{ cm}^{-1}$  (C=O stretching band), and  $1645\text{ cm}^{-1}$  (C=C bond in the PVP polymer backbone) provided further evidence of successful PVP loading into SiO<sub>2</sub> shells [56]. The increased C=C peak is attributed to the formation of a graphitic carbon structure during hydrothermal treatment, resulting from polymerization and crosslinking reactions of PDA and PEI polymers. Moreover, a broad and intense absorption band spanning  $788\text{--}1095\text{ cm}^{-1}$  (highlighted in yellow in Figure 7), corresponding to symmetric and asymmetric stretching of Si-O-Si bands, and a Si-OH peak at  $947\text{ cm}^{-1}$  present in all samples further affirmed the complete condensation of the APTES/TEOS precursor and the formation of the SiO<sub>2</sub> shell [44,56].

The reaction mechanism between the chosen PVP K30 molecules and the synthesized SiO<sub>2</sub> shells involves a combination of physical adsorption and chemical bonding. PVP, a water-soluble polymer, typically undergoes adsorption on the SiO<sub>2</sub> surface through hydrogen bonding and Van der Waals forces in an aqueous environment. The oxygen atoms in the pyrrolidone ring of PVP K30 readily form hydrogen bonds with the hydroxyl groups on piranha-treated Si-OH, subsequently coated with SiO<sub>2</sub> from APTES and TEOS condensation. PVP K30 proves advantageous in preventing Ostwald ripening in high-surface energy SiO<sub>2</sub> nanoparticles. The hydrothermal treatment employed in this study promotes chemical bonding between PVP K30 and SiO<sub>2</sub> shells, as verified by FT-IR results,

where oxygen atoms of the pyrrolidone ring form coordination bonds with the surface silanol groups of APTES/TEOS-SiO<sub>2</sub>@Si.

It is noteworthy that the Si–O–Si band intensity exhibited a declining trend from sol-gel coating to etching. The initial decrease, upon the addition of PVP K30, was attributed to the formation of PVP-treated SiO<sub>2</sub> shells. Subsequent reduction in peak intensity occurred with the introduction of PDA–PEI, coinciding with the emergence of a robust C=C peak. Thermal treatment at 800 °C contributed to increased SiO<sub>2</sub> stability, evidenced by a slight increase in Si–O–Si band intensity. Eventually, a significant reduction in Si–O–Si band intensity ensued after NaOH etching, signifying the dissolution of the SiO<sub>2</sub> template.

TEM analysis, depicted in Figure 8, contrasts sample composites with and without PVP K30 surface protection, emphasizing carbon coating integrity and the preservation of spherical morphologies post-etching. As illustrated in Figure 8a,b, PVP K30 surface-protected composite samples exhibited exceptional stability, sustaining the PDA–PEI carbon network structure even after NaOH etching. In contrast, Figure 8c,d illustrates distinct morphological differences in composites lacking PVP K30 protection, where a substantial portion of PDA carbon shells was compromised, and sheet-like PEI carbon networks were disrupted.

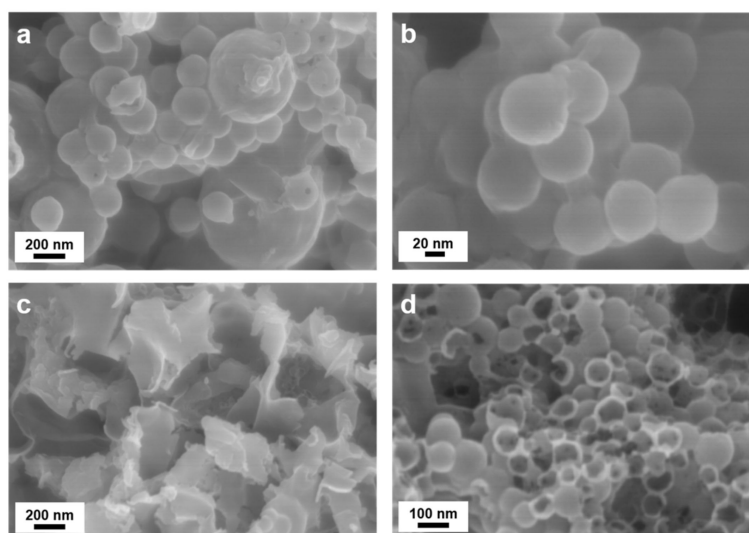


**Figure 8.** TEM images of composite samples fabricated via hydrothermal treatment of APTES/TEOS-SiO<sub>2</sub>@Si seeds (a,b) with or (c,d) without PVP K30 surface protection after NaOH etching.

The confirmation of PVP K30 polymer loading into APTES/TEOS-SiO<sub>2</sub>@Si was established through XPS analysis, as depicted in Figure 9. The survey spectra of PVP-SiO<sub>2</sub>@Si were compared with pristine Si nanoparticles (Figure S7 in Supplementary Materials). High-resolution Si 2p scans (Figure 9a) exhibited peaks at 104.11 eV, 102.75 eV, and 105.09 eV, corresponding to the Si–O–Si band. Si oxidation states (Si<sup>2+</sup>, Si<sup>3+</sup>, Si<sup>4+</sup>) indicated SiO<sub>2</sub> shell synthesis after APTES and TEOS condensation [61,63]. O 1s scans (Figure 9b) revealed peaks at 532.52 eV (Si–O–Si band) and 531.18 eV (C=O in PVP), while 529.84 eV (C–O), 533.38 eV (O–C=O), and 529.84 eV (O–C=O) were attributed to carbon-containing groups of silane precursors [62]. Peaks at 283.53 eV, 285.08 eV, 286.61 eV, and 288.34 eV in the C 1s (Figure 9c) scans indicated PVP molecular structure contributions [68]. The N 1s scan (Figure 9d) at 400.07 eV identified N atoms from C–N in the APTES structure. These XPS results substantiate the successful incorporation of PVP K30 into APTES/TEOS-SiO<sub>2</sub>@Si.

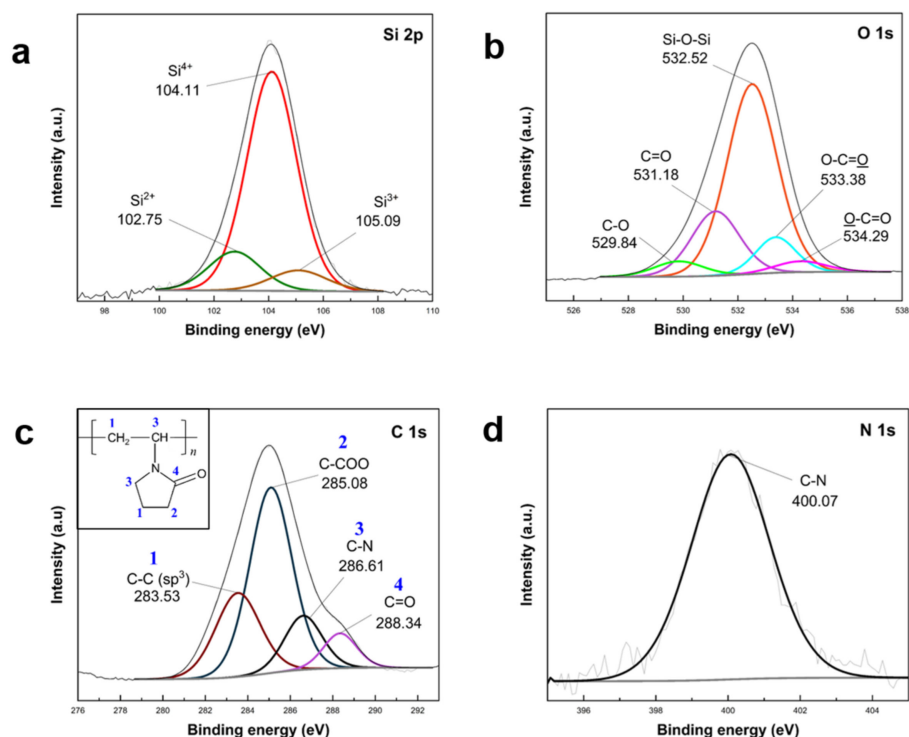


**Figure 9.** XPS high-resolution (a) Si 2p, (b) O 1s, (c) C 1s, and (d) N 1s scans of APTES/TEOS-SiO<sub>2</sub>@Si after PVP K30 polymer loading via the proposed hydrothermal route. The inset in (c) shows different carbon atoms in the PVP K30 molecular structure.

### 3.4. Characterization of Representative Core Shell and Yolk Shell Composites

Representative composites including core shell and yolk shell formations were synthesized following the proposed route, with one sample featuring PVP-protected SiO<sub>2</sub> shells and PEI-crosslinked structure. Surface composition changes in these structures (core shell PDA-PEI@SiO<sub>2</sub>@Si and yolk shell PDA-PEI@SiO<sub>2</sub>@Si) were investigated using XPS analysis. High-resolution scans are depicted in Figure 10, and survey spectra of the composites are provided in Figure S8 (Supplementary Materials).

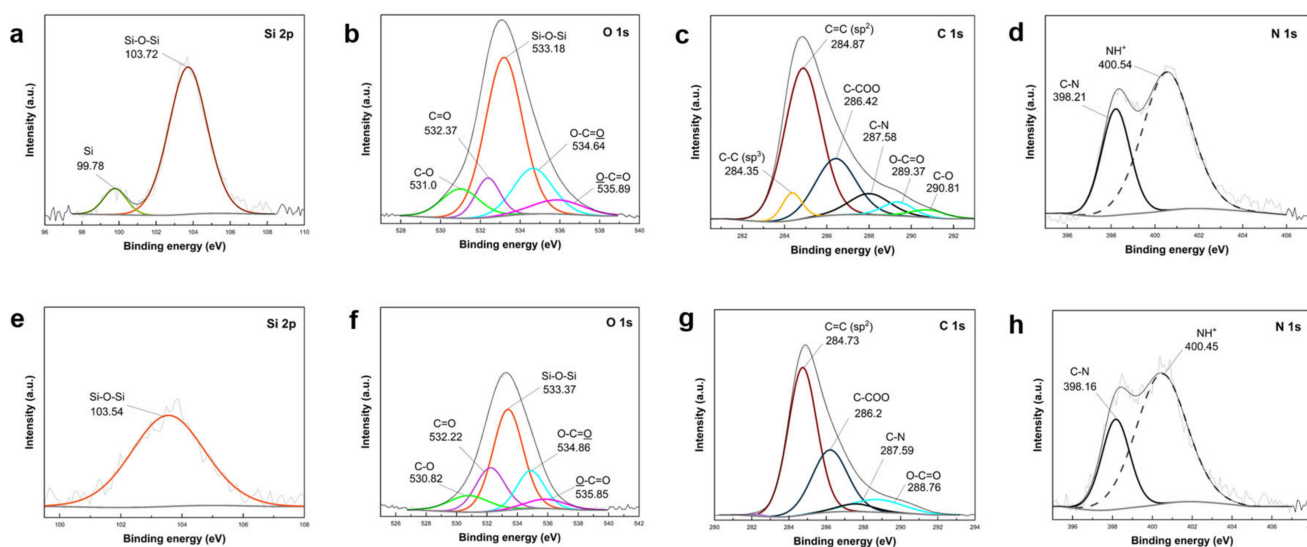


**Figure 10.** XPS high-resolution (a,e) Si 2p, (b,f) O 1s, (c,g) C 1s, and (d,h) N 1s scans of (a–d) core shell PDA-PEI@SiO<sub>2</sub>@Si and (e–h) yolk shell PDA-PEI@SiO<sub>2</sub>@Si composite samples.

The high-resolution Si 2p scan of the core shell PDA-PEI@SiO<sub>2</sub>@Si composite (Figure 10a) exhibited two distinct peaks at 103.72 eV and 99.78 eV. The peak at 103.72 eV was attributed to the Si-O-Si band, displaying a higher intensity compared to the peak at 99.78 eV assigned to Si [61]. These peaks align well with the reported literature. Deconvolution of the O 1s scans (Figure 10b) revealed five components at 533.18 eV (Si-O-Si), 534.64 eV (O-C=O), 532.37 eV (C=O), 531.0 eV (C-O), and 535.89 eV (O-C=O) in decreasing order of intensity [62,65]. Additionally, the C 1s scan displayed peaks at 284.87 eV (sp<sup>2</sup> C=C), 286.42 eV (C-COO), 289.37 eV (C-N), 284.35 eV (sp<sup>3</sup> C-C), 289.37 eV (O-C=O), and 290.81 eV (C-O) [64,69].

The yolk shell PDA-PEI@SiO<sub>2</sub>@Si sample displayed analogous peaks with reduced intensities compared to the core shell counterpart, primarily due to NaOH etching. As shown in Figure 10e, the Si 2p scan revealed a reduced intensity in the Si-O-Si band at 103.54 eV, and the O 1s scans (Figure 10f) displayed diminished intensities for Si-O-Si (533.37 eV), O-C=O (534.86 eV), C=O (532.22 eV), O-C=O (535.85 eV), and C-O (530.82 eV). However, the sp<sup>3</sup> C-C and C-O peaks in the C 1s scan of the core shell composite (Figure 10c) disappeared in the yolk shell composite (Figure 10g) after SiO<sub>2</sub> removal, indicating the destruction of carbon structures. This was consistent with Figure 8 TEM images for composites lacking PVP K30 surface protection. Detected chemical species in O 1s scans aligned well with C 1s results, attributed to SiO<sub>2</sub>, carbon-containing ligands, PDA carbon coating, and PEI crosslinks.

In the N 1s scan of the core shell PDA-PEI@SiO<sub>2</sub>@Si sample (Figure 10d), two peaks were observed at 400.54 eV and 398.21 eV. Similarly, in the yolk shell PDA-PEI@SiO<sub>2</sub>@Si sample, these peaks appeared at 400.45 eV and 398.16 eV. These peaks were attributed to protonated amines resulting from APTES hydrolysis and C-N bonds, respectively [65]. The C-N bond, detected in O 1s, C 1s, and N 1s scans, signified the crosslinking reaction between amino groups and catechol in oxidized PDA polymer chains with PEI molecules. The expected formation of PDA-PEI networks was supported by Schiff base or Michael addition reactions, illustrated in Figure S9 (Supplementary Materials) [70].

XPS results (Figure 11) underscore the impact of PVP K30 and the contributions of PEI crosslinks in reinforcing carbon coating durability in the core shell PDA@SiO<sub>2</sub>@Si versus yolk shell PDA-PEI@PVP-SiO<sub>2</sub>@Si composite. The corresponding survey spectra are provided in Figure S10 (Supplementary Materials).

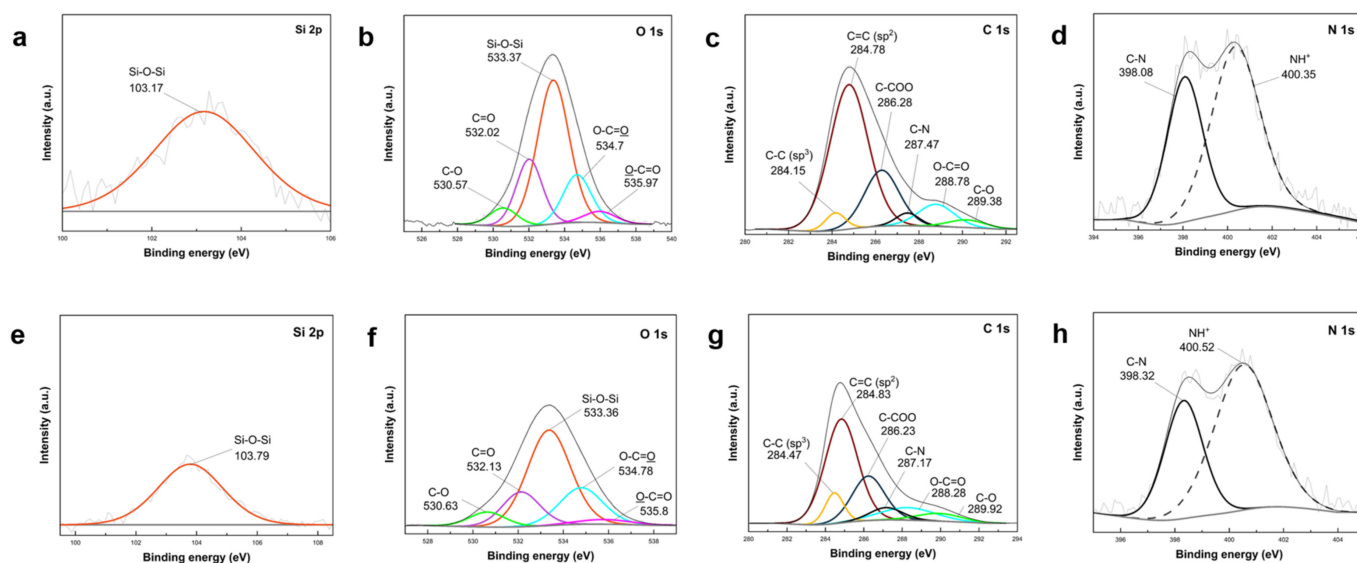


**Figure 11.** XPS high-resolution (a,e) Si 2p, (b,f) O 1s, (c,g) C 1s, and (d,h) N 1s scans of (a–d) core shell PDA@SiO<sub>2</sub>@Si and (e–h) yolk shell PDA-PEI@PVP-SiO<sub>2</sub>@Si composite samples.

Similar peak characteristics were identified in both composite samples. For instance, the Si 2p spectra of the core shell PDA@SiO<sub>2</sub>@Si in Figure 11 exhibited a Si–O–Si band, mirroring the presence of this band in the yolk shell PDA–PEI@PVP–SiO<sub>2</sub>@Si sample (Figure 11e), albeit with a slightly diminished intensity. Correspondingly, O 1s scans (Figure 11b,f) for both samples revealed comparable chemical compositions with analogous binding energies, including Si–O–Si, C=O, C–O–C, C–O, and O–C=O, in order of decreasing peak intensities. C 1s scans (Figure 11c,g) for both samples demonstrated consistent peaks for sp<sup>2</sup> C=C, C–COO, C–N, O–C=O, and C–O. Additionally, N 1s scans (Figure 11d,h) showed no substantial variations between the two composites. Despite the reduced peak intensities of O-containing groups in PDA–PEI@PVP–SiO<sub>2</sub>@Si due to etching, noteworthy sustenance of the sp<sup>3</sup> C–C peak at 284.47 eV and C–O peak at 289.92 eV in the C 1s spectrum (Figure 11g) emphasized the pivotal role of PVP surface protection and PEI crosslinking in constructing a resilient carbon coating capable of withstanding NaOH etching during template removal.

Raman spectroscopy was performed to determine defect quantity within the carbon coating layer and identify the degree of graphitization of representative core and yolk shell composites. TEOS–SiO<sub>2</sub>@Si, APTES/TEOS–SiO<sub>2</sub>@Si and PVP–SiO<sub>2</sub>@Si samples were also analyzed for reference purposes. Recorded spectra of each representative composite and reference samples are summarized in Figure 12.

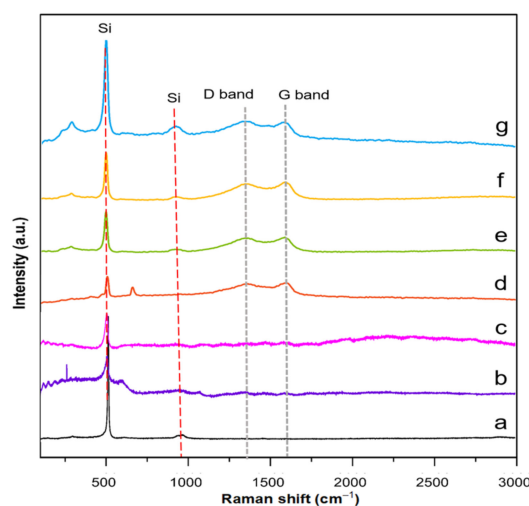


**Figure 12.** Raman spectra of (a) TEOS–SiO<sub>2</sub>@Si, (b) APTES/TEOS–SiO<sub>2</sub>@Si, (c) PVP–SiO<sub>2</sub>@Si, (d) core shell PDA@SiO<sub>2</sub>@Si, (e) yolk shell PDA–PEI@SiO<sub>2</sub>@Si, (f) yolk shell PDA–PEI@PVP–SiO<sub>2</sub>@Si, and (g) core shell PDA–PEI@SiO<sub>2</sub>@Si samples.

The recorded Raman spectra depicted characteristic peaks at 511 cm<sup>−1</sup> and 918 cm<sup>−1</sup>, indicative of Si, across all samples, affirming the preservation of Si crystallinity and intrinsic features. Notably, the Si peak intensity exhibited a decline following APTES addition, suggesting the formation of an amorphous SiO<sub>x</sub> layer around Si. A further reduction in Si peak intensity occurred upon PVP loading onto SiO<sub>2</sub> shells. All representative composite samples exhibited discernible D bands (~1350 cm<sup>−1</sup>) and G bands (~1590 cm<sup>−1</sup>), typical of sp<sup>2</sup>-bonded carbons in graphite and related structures after the pyrolysis of PDA and PEI molecules [71]. Second-order vibrations around ~2400 cm<sup>−1</sup> observed in PDA–PEI-containing composites indicated the partial graphitization of the carbon coating [72]. Stronger G bands compared to D bands across composites suggested the integration of PDA and PEI into a crystalline graphitic matrix, in alignment with TEM findings. The I<sub>D</sub>/I<sub>G</sub> ratio, quantified after curve fitting using a Gaussian–Lorentzian model, reinforced these observations, as detailed in Figures S11–S14 and Table S1 (Supplementary Materials) [73].

The increase in the I<sub>D</sub>/I<sub>G</sub> value from core shell PDA@SiO<sub>2</sub>@Si (0.84) to core shell PDA–PEI@SiO<sub>2</sub>@Si (0.85) is attributed to increased sp<sup>2</sup>-carbon edge atoms resulting from the

co-polymerization of PDA and PEI, followed by graphitization during thermal treatment. A parallel increase in the  $I_D/I_G$  value for yolk shell PDA-PEI@SiO<sub>2</sub>@Si (0.85) suggests successful carbonization of polymer coatings. In contrast, PVP-SiO<sub>2</sub>@Si exhibited minimal variations in the  $I_D/I_G$  ratio, potentially due to the dominant Si signals masking the carbon contribution from PVP K30. Yolk shell PDA-PEI@PVP-SiO<sub>2</sub>@Si (0.86) displayed the highest  $I_D/I_G$  value, indicating PDA-PEI graphitization and the subsequent carbonization of PVP K30, offering protective properties to SiO<sub>2</sub> shells after thermal treatment [74].

Figure 13 displays TG/DTA thermograms, including DTG curves, of representative composites that were subjected to controlled combustion up to 800 °C under N<sub>2</sub> gas protection.

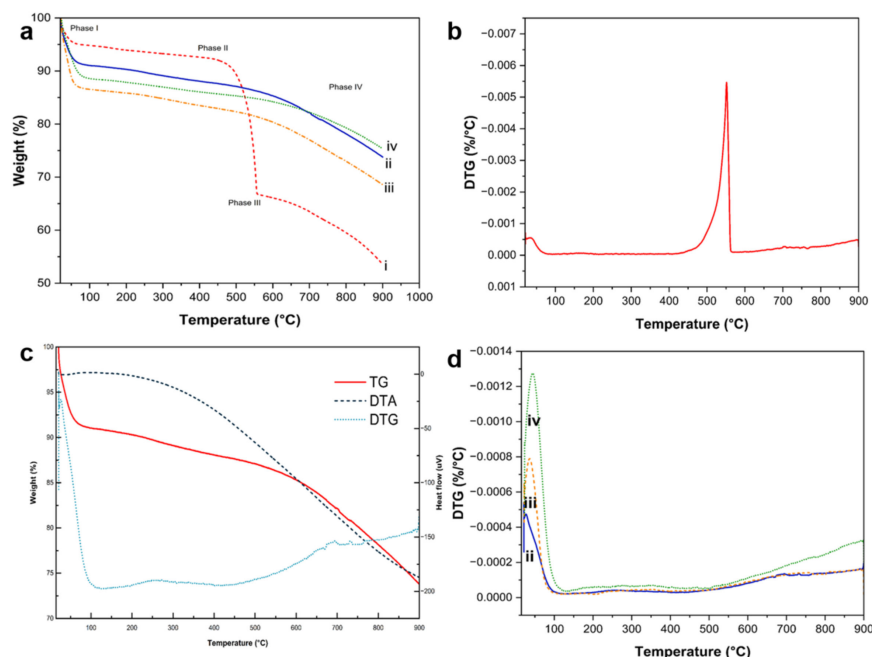


**Figure 13.** (a) TG curves of (i) core shell PDA@SiO<sub>2</sub>@Si, (ii) yolk shell PDA-PEI@PVP-SiO<sub>2</sub>@Si, (iii) yolk shell PDA-PEI@SiO<sub>2</sub>@Si, and (iv) core shell PDA-PEI@SiO<sub>2</sub>@Si samples. (b) TG-DTA and DTG curves of representative composite (ii). (c) DTG curves of (i) and (d) (ii-iv) composites.

TG profiles depicted in Figure 13a delineate four distinct phases based on the composition of representative samples. Phase I, characterized by a slight decrease in sample weight at approximately 50–90 °C, was attributed to the loss of physisorbed water on the composite surface. The subsequent phase involved the decomposition of polymers, extending broadly up to around 220 °C. In Phase II, a gradual weight loss occurred within the temperature range of ~400–550 °C. Notably, the core shell PDA@SiO<sub>2</sub>@Si sample exhibited a sharp decline in weight, indicative of rapid PDA coating degradation without the assistance of PEI crosslinks or PVP K30 molecules. This observation was corroborated by the DTG profile in Figure 13b. The calculated total carbon content for the core shell PDA@SiO<sub>2</sub>@Si sample was approximately 60 wt.%, consistent with the fabrication ratio. Phase III commenced at ~550 °C, marked by sample weight loss due to the oxidation of exposed Si particles that were vulnerable to elevated temperatures [32]. The oxidation reaction persisted into Phase IV, concluding at ~700 °C when all sample components combusted, leaving Si and SiO<sub>x</sub> components. Remarkably, composites with either PEI crosslinking or PVP K30 surface protection exhibited superior thermal stability, with minimal sample weight loss at temperatures exceeding 550 °C, emphasizing the effectiveness of the PDA carbon coating reinforced by PEI crosslink structures.

The enhanced thermal stability of PDA-PEI co-polymerized coating structures was validated through the DT-TGA and DTG curves of the representative yolk shell PDA-PEI@PVP-SiO<sub>2</sub>@Si composite samples, as depicted in Figure 13c. The TG curve exhibited a

consistent and sharp weight loss of approximately 10%, corresponding to the removal of both physisorbed and chemisorbed water. Additionally, the TG curve displayed a small exothermic peak around 100 °C, attributed to moisture loss, a broad endothermic peak centered at 200–400 °C signifying polymer decomposition, and a broad exothermic signal emerging from 500 °C due to SiO<sub>2</sub> oxidation. The DTG curve further illustrated water removal from a small endothermic peak at ~100 °C and actual polymer degradation from a broad endothermic peak within the range of ~200–400 °C. The decomposition of carbon components was confirmed by a broad exothermic signal spanning ~400–550 °C, while endothermic peaks at ~700 °C indicated the transition into SiO<sub>x</sub> [75].

Apart from a minor weight loss observed at ~50–100 °C due to the evaporation of adsorbed water molecules, depicted in Figure 13b, no substantial changes in sample weights were noted at 550 °C for the remaining composite samples, as illustrated in Figure 13d. The complete combustion of carbon-based compounds typically occurs from ~400–550 °C. However, the representative yolk shell PDA–PEI@PVP–SiO<sub>2</sub>@Si composite only exhibited a slight decrease in sample weight at ~700 °C, suggesting that the composite fabrication and design effectively prevented the thermal oxidation of Si. Based on sample weight loss, the total carbon content in yolk shell PDA–PEI@PVP–SiO<sub>2</sub>@Si was calculated to be ~18%, while the silicon content was ~73%, stemming from the combined contributions of SiO<sub>2</sub> from APTES, TEOS, and pure Si nanoparticles.

### 3.5. Electrochemical Performances of Representative Core Shell and Yolk Shell Composites

The electrochemical performances of representative yolk and core shell composite samples were first characterized by CV. The results are presented in Figure 14.

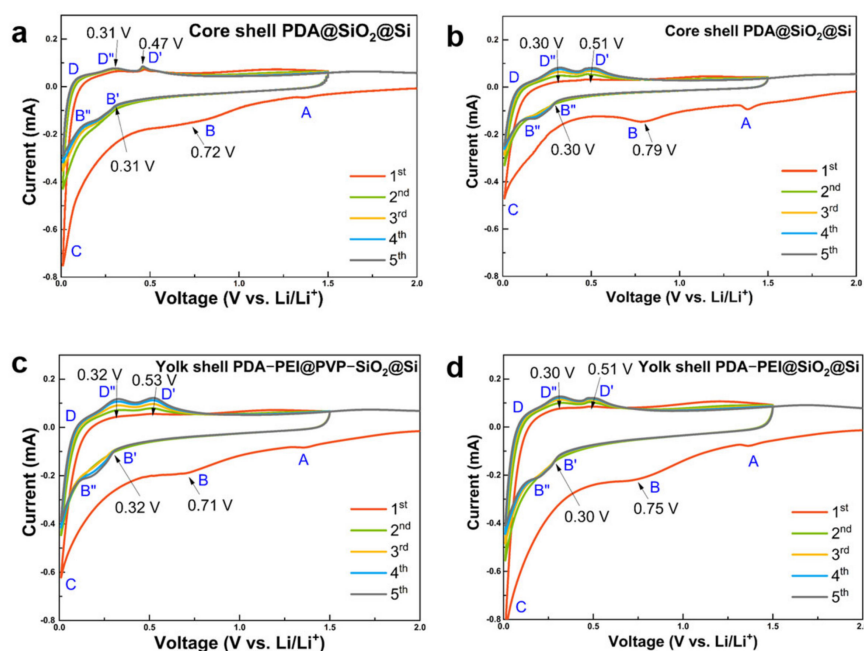


**Figure 14.** CV profiles of (a) core shell PDA@SiO<sub>2</sub>@Si in RT, (b) core shell PDA@SiO<sub>2</sub>@Si in HT, (c) yolk shell PDA–PEI@PVP–SiO<sub>2</sub>@Si in HT, and (d) yolk shell PDA–PEI@SiO<sub>2</sub>@Si in HT during the initial five cycles.

All composite samples demonstrated two distinct peaks at 0.30–0.32 V and 0.72–0.79 V during the first cathodic scan. They were ascribed to initial electrochemical reactions between bulk Si and Li<sup>+</sup> atoms which led to formation of irreversible lithiated precipitates. Si phase transformations and corresponding chemical reactions are summarized in Table 1 [37].

**Table 1.** Summary of phase transformations in Si nanoparticles during the first initial five cycles [37] \*.

Point in Figure 14	Phase Transformation	Chemical Reaction
A	SEI formation	$\text{Si} + x\text{Li}^+ + xe^- \rightarrow \text{Li}_x\text{Si}; x \leq 4$
B	Lithiation of crystalline Si (c-Si)	$\text{c-Si} + x\text{Li} \rightarrow \text{a-Li}_x\text{Si}$
C	Transformation to a new phase at <50 mV	$\text{a-Li}_x\text{Si} \rightarrow \text{a-Li}_y\text{Si}$
D	Delithiation of the phase formed at <50 mV	$\text{a-Li}_y\text{Si} \rightarrow \text{a-Li}_{x'}\text{Si} + (y - x')\text{Li}$
B'	Lithiation of amorphous Si (a-Si) at >0.17 V	$\text{a-Si} + x'\text{Li} \rightarrow \text{a-Li}_{x'}\text{Si}$
B''	Lithiation of a-Si between 70 mV and 0.17 V	$\text{a-Li}_{x'}\text{Si} + x''\text{Li} \rightarrow \text{a-Li}_{(x'+x'')}\text{Si}$
D''	Delithiation of a-Si at <0.38 V	$\text{a-Li}_{(x'+x'')}\text{Si} \rightarrow \text{a-Li}_{x'}\text{Si} + x''\text{Li}$
D'	Delithiation of a-Si at >0.38 V	$\text{a-Li}_{x'}\text{Si} \rightarrow \text{a-Si} + x'\text{Li}$

\* Note: From “Characteristics and Electrochemical Performance of Hydroxyl-Functionalized Graphene Quantum Dot-Coated Si Nanoparticles/Reduced Graphene Hybrid Anodes for Advanced Li-Ion Batteries,” by A. Martino, R. Cong, M. Jo., H.H. Park., H. Lee and C.S. Lee, 2023, J. Nanomater., 2023, Article ID 6353894, p. 15, Results section, Table 1 (<https://doi.org/10.1155/2023/6353894>) accessed on 23 January 2024. CC BY.

The disappearance of cathodic peaks between 0.72 V and 0.79 V in the second cycle indicates the stabilization of the SEI film after the initial cycle. Subsequent anodic scans revealed two broad oxidation peaks centered at 0.47–0.53 V and 0.30–0.32 V, signifying the delithiation processes of  $\text{Li}_{4.2}\text{Si}$  and the complete delithiation into amorphous Si ( $\text{Li}_x\text{Si}$ ), respectively. While the core shell PDA@SiO<sub>2</sub>@Si sample exhibited less polarization (Figure 14a), hydrothermally fabricated counterparts (Figure 14b) demonstrated electrode activation with a gradual increase in the intensities of both cathodic and anodic scans in subsequent cycles. Similarly, PVP-surface-protected composites (Figure 14c) showed gradual electrode activation compared to their less polarized counterparts (Figure 14d). Additionally, cyclic voltammetry (CV) scans of the core shell PDA-PEI@TEOS-SiO<sub>2</sub>@Si composite at room temperature (Figure S11) displayed similar peak observations and qualities, although key oxidation peaks during the delithiation process were not clearly manifested, suggesting challenges in retrieving Li<sup>+</sup> from  $\text{Li}_x\text{Si}$  alloyed components during the reaction.

Figure 15 illustrates electrochemical performances, including cycling stability, rate performance, and Coulombic efficiency, over 100 cycles. Additional charge/discharge profiles are in Figure S16 (see Supplementary Materials).

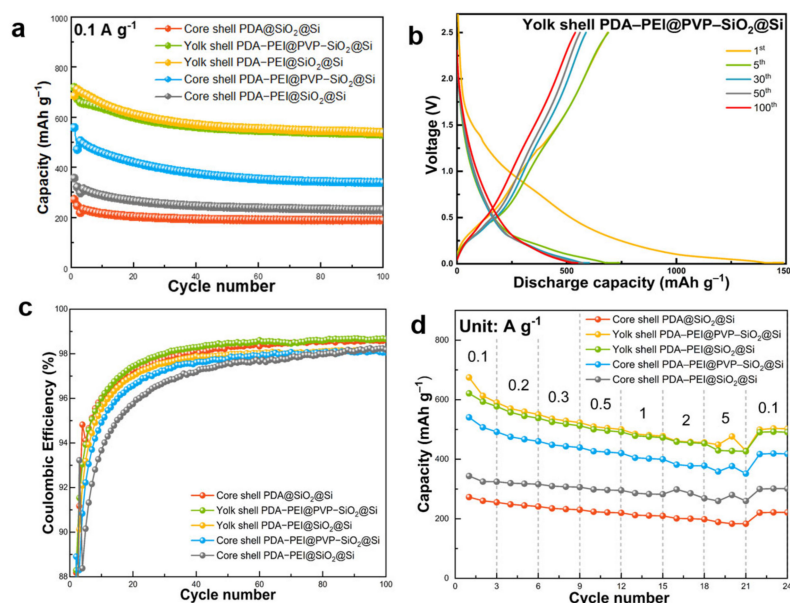


**Figure 15.** (a) Cycling performances of composite samples with (b) galvanostatic charge and discharge profiles of representative yolk shell PDA-PEI@PVP-SiO<sub>2</sub>@Si composite sample via HT. (c) Corresponding CE values of composite samples at 0.1 A g<sup>-1</sup> over 100 lithiation/delithiation cycles. (d) Rate performances of representative composite samples.

Electrochemical performances of core shell, yolk shell structures, and PVP surface-protected PDA-PEI@PVP-SiO<sub>2</sub>@Si were evaluated at 0.1 A g<sup>-1</sup> for 100 cycles (Figure 15a). The yolk shell composite demonstrated superior discharge capacity, starting at 719 mAh g<sup>-1</sup> with an initial Coulombic efficiency (ICE) of 47.94%. ICE increased to 94% after five cycles and consistently exceeded 98% in subsequent cycles.

The observed phenomenon of low ICE followed by a significant increase in the second cycle for Si-based anodes is linked to the formation and stabilization of the SEI layer. This behavior, known as SEI activation, involves an irreversible and necessary consumption of Li<sup>+</sup> during the initial cycles. In the first discharge cycle, Li<sup>+</sup> is intercalated into the Si electrode structure, resulting in the formation of lithiated precipitates. The expansion and contraction of the Si volume induce mechanical stress, causing morphological pulverization and SEI layer breakdown. Cracks in the Si morphology lead to the construction of a new SEI layer, consuming additional Li<sup>+</sup> and contributing to reduced reversible Li<sup>+</sup> availability during subsequent charging cycles. As the lithiation and delithiation cycles progress, the SEI undergoes stabilization, becoming more robust and protective. After SEI layer stabilization, the Si anode attains enhanced stability, facilitating the more effective storage and release of Li<sup>+</sup>, thereby improving CE values in subsequent cycles.

The galvanostatic charge and discharge profiles of the exemplary composite, as depicted in Figure 15b, exhibited minimal electrode polarization with overlapping profile scans across increasing cycle numbers. The low ICE of Si-based anodes is typically attributed to the decomposition reaction at the SEI layer, consuming Li<sup>+</sup> and diminishing available reversible Li<sup>+</sup> during initial cycles. The representative yolk shell PDA-PEI@PVP-SiO<sub>2</sub>@Si sample demonstrated a discharge capacity of 539.44 mAh g<sup>-1</sup> after 100 cycles, achieving a CE of 98%. Moreover, the CE stabilized after the initial SEI formation, as illustrated in Figure 15c.

The yolk shell structures performed better than its core shell counterparts in terms of cycling performance and CE stability at low-current density conditions for 100 cycles. Comparing the yolk shell PDA-PEI@SiO<sub>2</sub>@Si composite sample without PVP K30 and the representative composite PDA-PEI@PVP-SiO<sub>2</sub>@Si sample, the PDA-PEI@PVP-SiO<sub>2</sub>@Si sample was able to maintain 539.44 mAh g<sup>-1</sup>, only slightly higher than the 531.25 mAh g<sup>-1</sup> of yolk shell PDA-PEI@SiO<sub>2</sub>@Si after 100 cycles.

Meanwhile, even with the help of PVP K30 surface protection, the core shell PDA-PEI@PVP-SiO<sub>2</sub>@Si composite sample demonstrated inferior cycling performance with a capacity of only 339.62 mAh g<sup>-1</sup> after 100 cycles. This result highlights that the role of void spaces in yolk shell structures is sufficient in absorbing the internal volume changes of Si and stabilizing cycling performance. This result concludes that the PVP K30 polymer significantly affects the electrochemical performance of core shell samples at low-current density testing and yolk shell samples at high-rate loading.

The variations in cycling performance and CE between PDA-PEI@SiO<sub>2</sub>@Si and PDA@SiO<sub>2</sub>@Si composites, both featuring core shell structures, result from improved electronic conductivity in the former. This enhancement is attributed to PEI crosslinking throughout the electrode, establishing continuous pathways for rapid electron and ion transport.

Rate capabilities were assessed across various current densities (0.1 to 5 A g<sup>-1</sup>) for the composite samples, as depicted in Figure 15d. The yolk shell PDA-PEI@PVP-SiO<sub>2</sub>@Si electrode displayed superior rate performance compared to core shell composites, regardless of the presence of PVP K30 and PEI crosslinking, and exhibited no Li dendrite formation. At current densities of 0.1, 0.2, 0.3, 0.5, 1, 2, and 5 A g<sup>-1</sup>, specific capacities were 621.21, 577.46, 537.96, 512.50, 491.53, 472.71, and 453.16 mAh g<sup>-1</sup>, respectively. Upon returning to 0.1 A g<sup>-1</sup>, a specific capacity of 490.73 mAh g<sup>-1</sup> was regained.

While the yolk shell PDA-PEI@SiO<sub>2</sub>@Si composite exhibited slightly superior electrochemical performance compared to the representative yolk shell composite, a sudden capacity increase from 456.32 mAh g<sup>-1</sup> to 476.41 at 5 A g<sup>-1</sup> suggested a short circuit due to Li dendritic formations, common at high current densities. Similar abrupt capacity increases

were observed for core shell PDA-PEI@PVP-SiO<sub>2</sub>@Si and core shell PDA-PEI@SiO<sub>2</sub>@Si composites. It is noteworthy that slight capacity increases in other sample composites stabilized upon reducing the current density to 0.1 A g<sup>-1</sup>, indicating satisfactory recovery after high-rate tests.

Table 2 summarizes cycling and rate performances of the representative yolk shell PDA-PEI@PVP-SiO<sub>2</sub>@Si composite compared to other fabricated composites.

**Table 2.** Electrochemical performances of fabricated composites.

Composite Sample	Low-Current Density Performance (at 0.1 A g <sup>-1</sup> )						High-Current Density Performance				
	Discharge Capacity (mAh g <sup>-1</sup> )				CR *	CE	Discharge Capacity (mAh g <sup>-1</sup> )				
	1st	5th	99th	100th	100th	1st	5th	100th	1 A g <sup>-1</sup>	2 A g <sup>-1</sup>	5 A g <sup>-1</sup>
Core shell PDA@SiO <sub>2</sub> @Si	272.12	228.97	189.64	189.81	99.91	36.72	90.15	98.18	219.81	209.52	198.40
Core shell PDA-PEI@SiO <sub>2</sub> @Si	356.68	308.12	230.49	230.32	99.93	42.93	92.23	98.05	295.43	282.43	268.55
Core shell PDA-PEI@PVP-SiO <sub>2</sub> @Si	558.84	487.07	339.62	339.19	99.87	46.11	93.18	98.20	420.50	399.83	378.30
Yolk shell PDA-PEI@SiO <sub>2</sub> @Si	685.87	653.51	531.90	531.25	99.88	47.15	94.11	98.64	484.92	460.76	453.32
Yolk shell PDA-PEI@PVP-SiO <sub>2</sub> @Si	719.11	689.45	539.98	539.44	99.90	47.94	93.93	98.70	491.53	472.71	453.16

\* Capacity retention (CR) was calculated as measured discharge capacity of cycle  $n + 1$  divided by the measured discharge capacity of previous cycle  $n$ .

Electrochemical impedance measurements were conducted before and after the 100th cycle to elucidate factors contributing to the enhanced Li<sup>+</sup> storage capacity of the representative yolk shell PDA-PEI@PVP-SiO<sub>2</sub>@Si composite. Presented in Figure 16 are Nyquist plots, with insets (Figure 16a,b) illustrating corresponding equivalent circuit models. The circuit model considered the resistance values denoted as  $R_s$ ,  $R_{SEI}$ ,  $R_{CT}$ , and Warburg impedance ( $W_z$ ), representing the interactions of the electrolyte solution with bulk Si, Li<sup>+</sup> migration through the SEI layer, charge transfer resistance, and Warburg diffusion, respectively. Additionally, double-layer capacitances (CPE1 and CPE2) represented constant phase elements of the cell surface film.

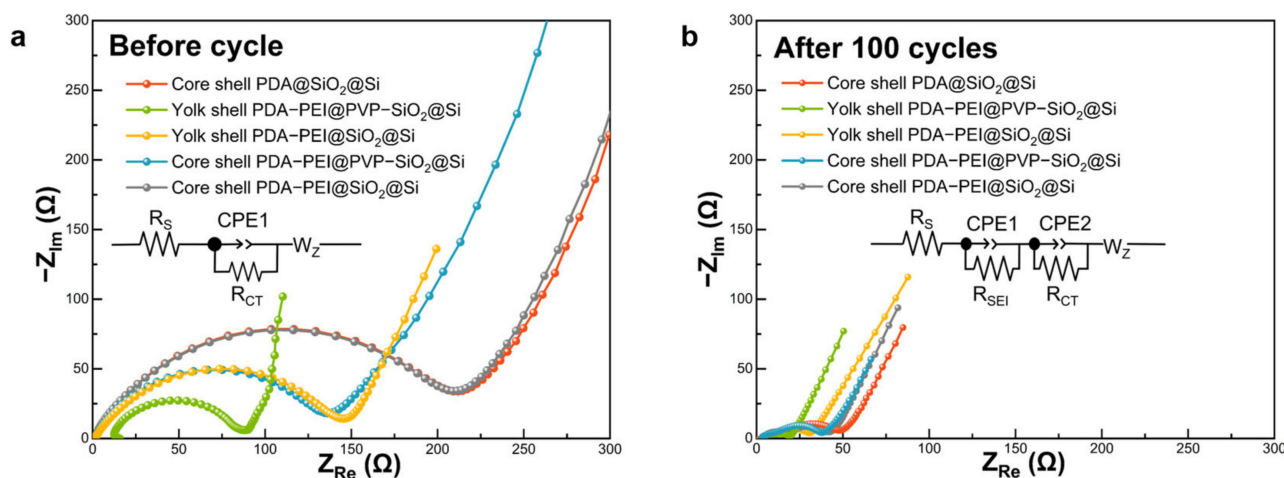


**Figure 16.** Nyquist plots and electrochemical impedance spectra of fabricated composites (a) before cycling and (b) after 100 lithiation/delithiation cycles (in scale).

As depicted in Figure 16a, Nyquist plots of the investigated composites before cycling exhibited a semicircle in the middle-frequency region and a slanted sloping line in

the low-frequency region. The smaller diameter of the representative yolk shell PDA-PEI@PVP-SiO<sub>2</sub>@Si before cycling indicated a lower R<sub>CT</sub> value (73.76 Ω), signifying faster charge transfer kinetics. This enhanced charge transfer could be attributed to the synergistic effect of the yolk shell structure, facilitating direct contact between the carbon coating layer and the PVP-SiO<sub>2</sub>@Si active material. Similarly, yolk shell PDA-PEI@SiO<sub>2</sub>@Si (139.60 Ω) and core shell PDA-PEI@PVP-SiO<sub>2</sub>@Si (140.21 Ω) demonstrated comparable R<sub>CT</sub> values, significantly lower than core shell PDA@SiO<sub>2</sub>@Si (211.16 Ω) and core shell PDA-PEI@SiO<sub>2</sub>@Si (209.23 Ω). The presence of a thick layer of amorphous SiO<sub>2</sub> coating in core shell composites hindered direct contact between the Si active material and the conductive PDA carbon coating, resulting in increased Li<sup>+</sup> tortuosity. In core shell composites, Li<sup>+</sup> migration needed to traverse the electronically insulating SiO<sub>2</sub> layer before reaching the Si active material, leading to a substantial increase in R<sub>CT</sub>.

Following 100 cycles, the formation of a stable SEI layer was confirmed in the Nyquist plots depicted in Figure 16b. The Nyquist plots for the fabricated electrodes exhibited two semicircles—one in the high-frequency region attributed to R<sub>SEI</sub> and the other in the middle-frequency region representing R<sub>CT</sub>—and a slanted line in the low-frequency region.

The representative composite displayed the smallest diameter in the high-frequency semicircle, indicating the lowest R<sub>SEI</sub> value (6.30 Ω). This reduction was attributed to the formation of a mechanically stable SEI layer facilitated by the PDA coating, preventing excessive electrolyte decomposition. Yolk shell PDA-PEI@SiO<sub>2</sub>@Si also exhibited a relatively lower R<sub>SEI</sub> value (8.13 Ω) compared to its core shell counterparts, underscoring the significance of the yolk shell structure. However, a larger R<sub>CT</sub> value for yolk shell PDA-PEI@SiO<sub>2</sub>@Si (19.28 Ω) compared to the representative composite (9.71 Ω) emphasized the importance of constructing yolk shell structures with PVP K30 surface protection. Core shell composites PDA-PEI@PVP-SiO<sub>2</sub>@Si (9.51 Ω) with PVP K30 demonstrated lower R<sub>SEI</sub> values than the PDA-PEI@SiO<sub>2</sub>@Si (10.77 Ω) sample, highlighting the efficacy of PVP K30 in enhancing the electrochemical performance.

The formation of a stabilized SEI film in core shell PDA-PEI@PVP-SiO<sub>2</sub>@Si can be elucidated by the influence of PVP K30 polymer chains when loaded into amorphous SiO<sub>2</sub> shells. In the event of crack formation in the PDA carbon coating due to the expansion of lithiated Si and SiO<sub>2</sub> components, the embedded PVP K30 polymer chains within SiO<sub>2</sub> shells act as a secondary barrier, preventing direct contact with Si active materials. Furthermore, the flexibility of PVP K30 polymer chains contributes to the stable formation of SEI by serving as a buffer against the rigid and dense SiO<sub>2</sub> layer, susceptible to crack formation during repetitive volume fluctuations. The incorporation of PVP K30 polymer chains within SiO<sub>2</sub> also enhances the conductivity of amorphous SiO<sub>2</sub> seeds, resulting in a slight improvement in the R<sub>CT</sub> of core shell PDA-PEI@PVP-SiO<sub>2</sub>@Si (23.32 Ω) compared to core shell PDA-PEI@SiO<sub>2</sub>@Si (28.01 Ω). Conversely, the absence of the PEI component in core shell PDA@SiO<sub>2</sub>@Si led to a higher R<sub>SEI</sub> (10.84 Ω) coupled with thick SiO<sub>2</sub> shells, obstructing Li<sup>+</sup> migration and increasing tortuosity (32.50 Ω).

Table 3 summarizes parameters acquired from Nyquist plots of fabricated composites before and after 100 lithiation/delithiation processes.

Long cycling performance stability at a high-rate loading of the fabricated composite electrode was evaluated at 1 A g<sup>-1</sup> for 200 lithiation/delithiation cycles. Cycling performances under prolonged cycling at a high-rate loading are illustrated in Figure 17.

As depicted in Figure 17a, the cycling behavior of hybrid anodes subjected to a high current density of 1 A g<sup>-1</sup> for 200 cycles mirrored trends observed in previous low-density cycles. In summary, initial discharge capacities for the yolk shell PDA-PEI@SiO<sub>2</sub>@Si, yolk shell PDA-PEI@PVP-SiO<sub>2</sub>@Si, core shell PDA-PEI@PVP-SiO<sub>2</sub>@Si, core shell PDA-PEI@SiO<sub>2</sub>@Si, and core shell PDA@SiO<sub>2</sub>@Si composite electrodes were 853.94, 767.07, 540.98, 344.56, and 324.26 mAh g<sup>-1</sup> (descending in magnitude), respectively. All composite electrodes exhibited an initial decline in discharge capacity attributed to irreversible SEI formation. Discharge capacity then stabilized in subsequent cycles. Following 200 lithiation/delithiation cycles, reversible capacities of 523.50, 512.76, 319.18,

229.02, and 227.55 mAh g<sup>-1</sup> (in descending order) were achieved for corresponding composite electrodes.

**Table 3.** Comparison of fitted parameters obtained from Nyquist plots of studied composites.

Composite Sample	Resistance before Cycling ( $\Omega$ )			Resistance after 100 Cycles ( $\Omega$ )		
	$R_s$	$R_{SEI}$	$R_{CT}$	$R_s$	$R_{SEI}$	$R_{CT}$
Core shell PDA@SiO <sub>2</sub> @Si	-	-	211.16	4.85	10.84	32.50
Core shell PDA-PEI@SiO <sub>2</sub> @Si	-	-	209.23	3.89	9.77	28.01
Core shell PDA-PEI@PVP-SiO <sub>2</sub> @Si	-	-	140.21	3.53	9.51	23.32
Yolk shell PDA-PEI@SiO <sub>2</sub> @Si	-	-	139.60	3.30	8.13	19.28
Yolk shell PDA-PEI@PVP-SiO <sub>2</sub> @Si	-	-	73.76	3.21	6.30	9.71

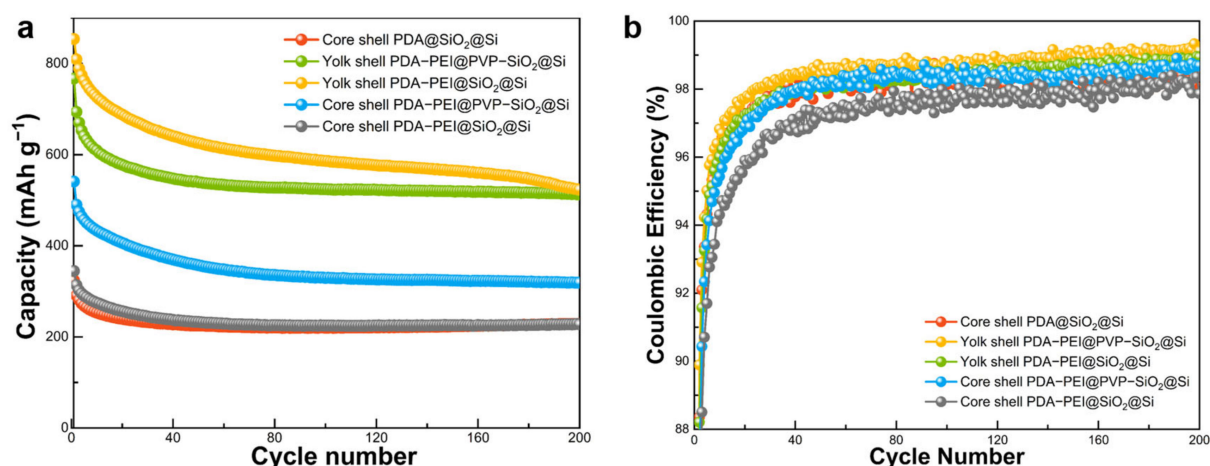


**Figure 17.** (a) Cycling performance and (b) CE of composite electrodes after 200 lithiation/delithiation cycles at a current density of 1 A g<sup>-1</sup>.

As representative yolk shell composite electrodes, specifically yolk shell PDA-PEI@SiO<sub>2</sub>@Si and yolk shell PDA-PEI@PVP-SiO<sub>2</sub>@Si displayed the highest initial discharge capacities of 853.94 and 767.07 mAh g<sup>-1</sup>, respectively. After 200 cycles, both electrodes exhibited stable cycling performance, retaining reversible capacities of 523.50 and 512.76 mAh g<sup>-1</sup>, respectively, showing minimal capacity losses. Although yolk shell PDA-PEI@SiO<sub>2</sub>@Si initially demonstrated a slightly higher discharge capacity, its cycling stability gradually declined after approximately 170 lithiation/delithiation cycles. In contrast, yolk shell PDA-PEI@PVP-SiO<sub>2</sub>@Si demonstrated a superior cycling performance, maintaining a relatively stable capacity retention rate during extended high-density cycling. This divergence in long-cycling performance was attributed to the significant influence of PVP K30 acting as a protective barrier between the PDA-PEI coating layer and SiO<sub>2</sub> shells during etching. Additionally, embedded PVP K30 polymer chains within SiO<sub>2</sub> shells contributed to a flexible silica structure, mitigating particle pulverization.

Figure 17b shows CE values of cycled samples at a high-rate loading. Notably, PDA-PEI@PVP-SiO<sub>2</sub>@Si, a representative yolk shell composite, exhibited the highest initial cycling efficiency (ICE) of 50.98% among investigated composites. Si-based composite anodes typically display low ICE values due to irreversible SEI formation, leading to Li<sup>+</sup> consumption and reduced reversible capacity. However, CE values exhibited an increasing trend after initial cycles, gradually stabilizing over subsequent cycles. After 200 cycles, the representative composite anode demonstrated the highest CE value of 99.12% among cycled samples.

The capacity contribution for each component (i.e., Si, SiO<sub>2</sub>, APTES, TEOS, PVP K30, PDA, and PEI) can be summarized as follows. Si, due to its excellent theoretical specific capacity, was used to boost the energy density of typical graphite-based commercial anodes.

SiO<sub>2</sub> was fabricated from APTES and TEOS dual template strategy to design a yolk shell structure to provide void spaces to buffer inevitable Si volume fluctuations. The APTES was used as a structure to regulate TEOS to facilitate monodispersed SiO<sub>2</sub> synthesis without a base catalyst and as a precursor to amino-functionalized SiO<sub>2</sub>. The PVP K30 polymers provided surface protection to prevent crack formation on the carbon coating and acted as a barrier that controls the rate of SiO<sub>2</sub> dissolution during the etching process. The PVP K30 polymers embedded within the SiO<sub>2</sub> shells also allowed for flexibility and conductivity to the rather amorphous and rigid SiO<sub>2</sub> shells. The PDA coating layer was designed to encapsulate the SiO<sub>2</sub>-coated Si active material and prevent direct electrolyte contact while mitigating the low conductivity of Si. Lastly, the crosslinking reaction between PDA and PEI contributed to the construction of a 3D, bubble wrap-like, interconnected porous matrix with a thermal stability reaching up to 700 °C. Each component in the representative yolk shell composite exhibited synergistic effects that resulted in a stable cycling performance with minimal capacity loss even after 200 cycles.

Table 4 provides a summary of cycling performances, including corresponding CE values, for the representative yolk shell PDA-PEI@PVP-SiO<sub>2</sub>@Si composite in comparison with other fabricated composites over an extended cycle period at a high-rate loading.

**Table 4.** Electrochemical performances of fabricated composites at 1 A g<sup>-1</sup> for 200 cycles.

Composite Sample	Discharge Capacity (mAh g <sup>-1</sup> )			CR *	CE		
	1st	100th	200th		1st	5th	200th
Core shell PDA@SiO <sub>2</sub> @Si	324.26	219.92	227.55	99.86	40.55	91.70	97.86
Core shell PDA-PEI@SiO <sub>2</sub> @Si	344.56	225.09	229.02	99.88	44.98	93.42	98.51
Core shell PDA-PEI@PVP-SiO <sub>2</sub> @Si	540.98	329.31	319.18	99.90	48.71	94.18	98.69
Yolk shell PDA-PEI@SiO <sub>2</sub> @Si	853.94	586.28	523.50	99.91	50.00	94.32	98.94
Yolk shell PDA-PEI@PVP-SiO <sub>2</sub> @Si	767.07	524.11	512.76	99.97	50.98	95.02	99.12

\* Capacity retention (CR) was calculated as measured discharge capacity of cycle  $n + 1$  divided by measured discharge capacity of previous cycle  $n$ .

The specific surface area and pore size distribution of the cycled composites were examined through BET analysis, as illustrated in Figure 18. The porous structure of the composites was elucidated using the BJH model. The N<sub>2</sub> adsorption-desorption isotherms of all obtained composites, as depicted in Figure 18a, exhibit the characteristic type IV adsorption isotherm with distinct hysteresis loops, signifying mesoporous structural features. The BET specific surface area ( $S_{\text{BET}}$ ) of the representative composites ranges from 220–650 m<sup>2</sup> g<sup>-1</sup>, with corresponding total pore volumes falling within the range of 0.12–0.67 cm<sup>3</sup> g<sup>-1</sup>, as summarized in Table S2 (see Supplementary Materials). The pore size distributions, calculated from the adsorption branch of the isotherms, reveal that the resulting composites possess a micro/mesoporous structure, with mesopores centered at approximately 2–4 nm, as depicted in Figure 18b.

The variation in specific surface areas among the investigated composites offers additional insights into the observed differences in electrochemical performance during prolonged cycling at high-rate loading. A higher specific surface area provides more active sites for the interaction between the electrode material and the electrolyte. The recorded  $S_{\text{BET}}$  values for the studied composites in ascending order were 224.56, 226.40, 409.05, 589.83, and 654.63 m<sup>2</sup> g<sup>-1</sup> for the core shell PDA@SiO<sub>2</sub>@Si, core shell PDA-PEI@SiO<sub>2</sub>@Si, core shell PDA-PEI@PVP-SiO<sub>2</sub>@Si, yolk shell PDA-PEI@SiO<sub>2</sub>@Si, and yolk shell PDA-PEI@PVP-SiO<sub>2</sub>@Si, respectively.

The BET analysis results indicate that the representative yolk shell PDA-PEI@PVP-SiO<sub>2</sub>@Si composite, characterized by the lowest pore volume (0.12 cm<sup>3</sup> g<sup>-1</sup>), highest  $S_{\text{BET}}$  value, and greatest specific surface area attributed to mesopores (570.96 m<sup>2</sup> g<sup>-1</sup>), exhibited the most stable electrochemical performance in terms of cycling and rate stability. The notable increase in the contact area enhanced the electrode-electrolyte interface, facilitating efficient ion transfer during both charging and discharging cycles. The high specific

surface area contributed to improved ion diffusion, allowing  $\text{Li}^+$  ions to traverse the electrode structure with reduced diffusion path lengths. Moreover, the extensive surface area of mesopores within the electrode structure helped distribute Si volume fluctuations effectively, thereby minimizing mechanical stress and mitigating issues related to electrode degradation over multiple cycles.

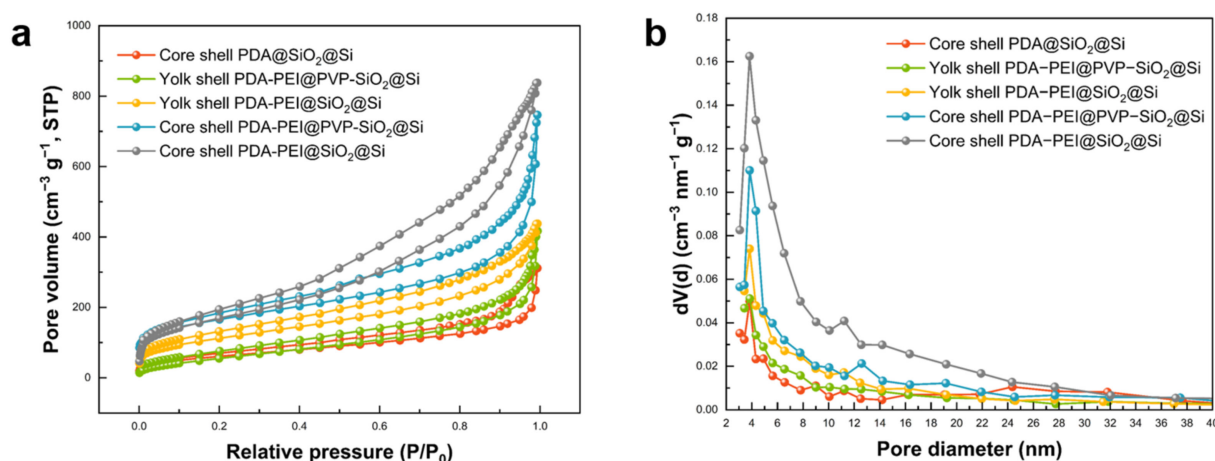


**Figure 18.** (a)  $\text{N}_2$  adsorption–desorption isothermals and (b) pore size distributions of the composite electrodes.

Achieving the right balance between optimal pore size and distribution was identified as crucial for the electrochemical performance of the other studied composites. Notably, the yolk shell PDA-PEI@SiO<sub>2</sub>@Si sample exhibited relatively higher specific surface areas of micropores with a small pore volume ( $0.13 \text{ cm}^3 \text{ g}^{-1}$ ), leading to limited  $\text{Li}^+$  diffusivity and compromised reversible capacity during high-rate loading over extended cycling (see Figure 17a, depicting capacity loss after 170 cycles). Conversely, core shell composites with high pore volumes and relatively higher specific surface areas of micropores than mesopores resulted in lower  $S_{\text{BET}}$  values and, consequently, lower reversible capacities under both cycling conditions.

To substantiate the electrochemical cycling stability of the investigated composites, we examined the surface topography of the fabricated anode materials before and after the 200th cycle at  $1 \text{ A g}^{-1}$  (Figure 19).

Prior to the initial cycle, electrode surfaces exhibited a sponge-like porosity, featuring aggregated SiO<sub>2</sub>@Si nanoparticles dispersed within interconnected carbon structures. Notably, Figure 19a illustrates a representative yolk shell PDA-PEI@PVP-SiO<sub>2</sub>@Si sample with a uniform surface without cracks, unlike the yolk shell PDA-PEI@SiO<sub>2</sub>@Si sample shown in Figure 19c, which displayed slight cracks despite sharing the same yolk shell structure. This distinction in surface morphology was attributed to enhanced flexibility conferred by the embedded PVP K30 polymer within the SiO<sub>2</sub>@Si shells in the representative composite. Similarly, Figure 19e demonstrates a comparable porous surface topography without cracks in the core shell PDA-PEI@PVP-SiO<sub>2</sub>@Si owing to the presence of the PVP K30 polymer during SiO<sub>2</sub> synthesis.

Conversely, the absence of PVP K30 polymer to provide flexibility to SiO<sub>2</sub> shells and PEI polymer for crosslinking between SiO<sub>2</sub>@Si nanoparticles was evident in Figure 19g (core shell PDA-PEI@SiO<sub>2</sub>@Si) and Figure 19i (core shell PDA@SiO<sub>2</sub>@Si). Both electrodes exhibited severe crack formation even before the lithiation/delithiation process. These cracks occurring between SiO<sub>2</sub>@Si aggregates impeded effective contact among active materials, resulting in compromised electrochemical performance, particularly in terms of discharge capacities.

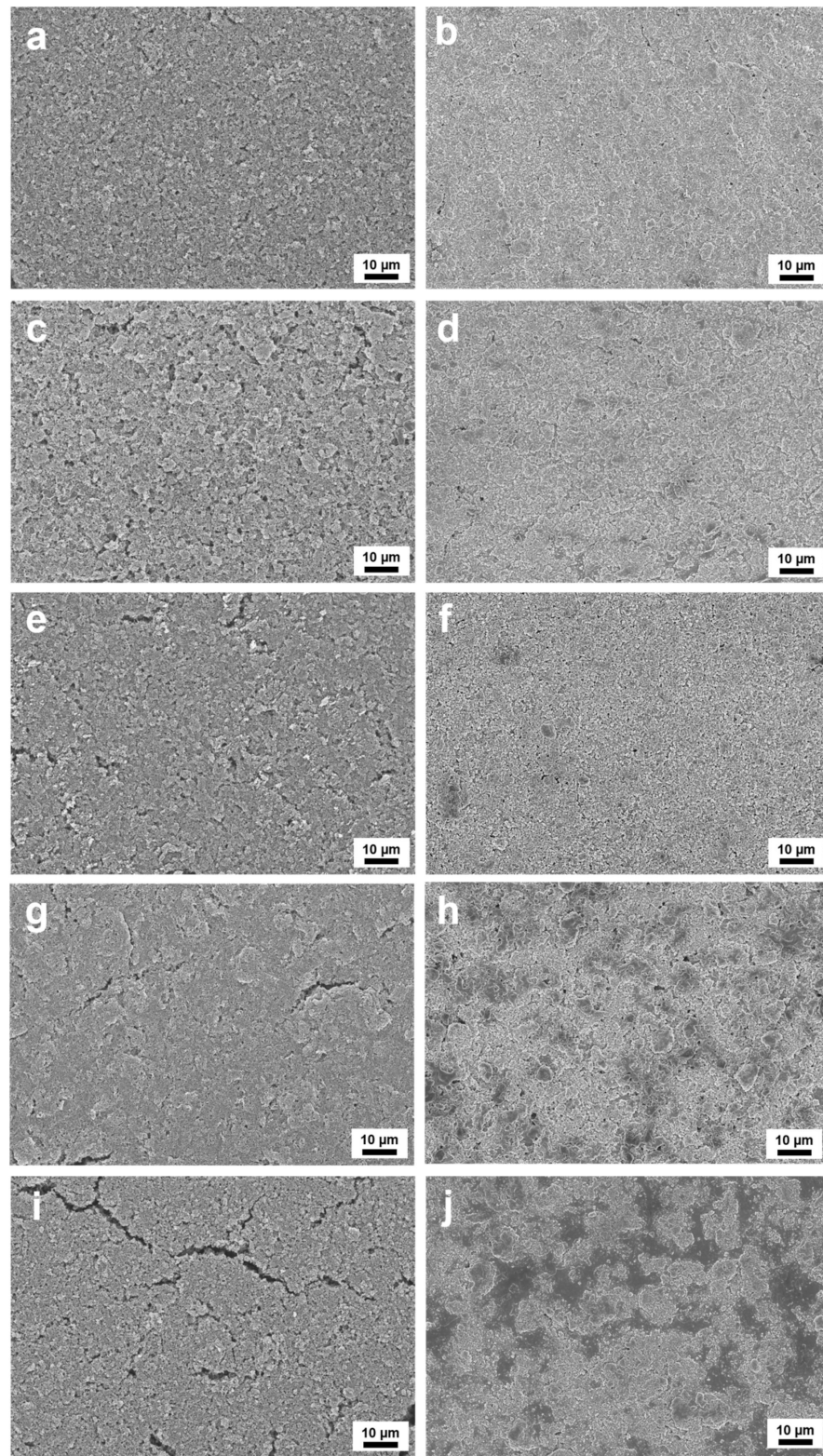


**Figure 19.** Representative SEM images showing surface view of (a,b) yolk shell PDA-PEI@PVP-SiO<sub>2</sub>@Si, (c,d) yolk shell PDA-PEI@SiO<sub>2</sub>@Si, (e,f) core shell PDA-PEI@PVP-SiO<sub>2</sub>@Si, (g,h) core shell PDA-PEI@SiO<sub>2</sub>@Si, and (i,j) core shell PDA@SiO<sub>2</sub>@Si anode before (a,c,e,g,i) and after (b,d,f,h,j) 200 lithiation/delithiation cycles at a current density of 1 A g<sup>-1</sup>.

Following 200 cycles at 1 A g<sup>-1</sup>, a smooth and crack-free surface of the representative composite electrode was found as shown in Figure 19b. Recurring electrochemical reactions

resulted in a thin layer covering active materials on the electrode surface. Both yolk shell PDA-PEI@SiO<sub>2</sub>@Si and core shell PDA-PEI@PVP-SiO<sub>2</sub>@Si samples displayed a similar surface topology, with pores initially present before cycling being filled with accumulated reaction by-products on the electrode surface (see Figure 19d and Figure 19f, respectively). In contrast, core shell PDA-PEI@SiO<sub>2</sub>@Si and core shell PDA@SiO<sub>2</sub>@Si samples exhibited severe surface cracks even before cycling due to the inflexible and unstable nature of their electrode structures. These cracks, filled with aggregated by-products (depicted by scattered gray areas in Figure 19h,j), exposed active Si nanoparticles to direct electrolyte parasitic decomposition, serving as nucleation sites for a thick and non-uniform SEI film after lithiation.

The electrochemical cycling stability of investigated composite anodes, even under high-rate loading, was confirmed by SEM images, which revealed negligible damage to the electrode structure. Figure S17 provides insights into the morphology of composites before and after cycling. The spherical configuration of active Si nanoparticles enveloped by carbon coating layers remained intact with minimal particle expansion. Notably, exposed SiO<sub>2</sub>@Si nanoparticles were not detected. The internal volumetric fluctuations of Si active material within the polymer carbon matrix were suppressed. Consequently, electrode structures exhibited sustained electrochemical cycling stability over 200 cycles.

#### 4. Conclusions

In summary, this study underscores the critical role of designing rattle-type yolk shell Si/C composite structures derived from APTES/TEOS dual templates, incorporating SiO<sub>2</sub> shells treated with PVP K30 polymers for surface protection against NaOH etching. These structures are encapsulated within a conformal PDA carbon coating layer and dispersed within a 3D cross-linked matrix resembling bubble wrap, formed using PEI polymers via a hydrothermally assisted modified Stöber process. The representative yolk shell composite, PDA-PEI@PVP-SiO<sub>2</sub>@Si, exhibited an initial discharge capacity of 719 mAh g<sup>-1</sup> and retained a capacity of 539 mAh g<sup>-1</sup> after 100 cycles at 0.1 A g<sup>-1</sup>. At a high current density of 5 A g<sup>-1</sup>, the composite maintained a capacity of 453 mAh g<sup>-1</sup> without Li dendritic formation. Over 200 cycles at 1 A g<sup>-1</sup>, the anode displayed excellent capacity retention, reaching a rate of 99.97% with a reversible capacity of 512.76 mAh g<sup>-1</sup>.

The superior electrochemical performance of the representative composite, compared to other investigated composites, stems from various synergistic factors in the proposed synthetic design. (1) the self-catalytic action of APTES, serving both as a structure-regulating agent for synthesizing spherical SiO<sub>2</sub> shells without a base catalyst and as a precursor to amino-functionalized SiO<sub>2</sub> shells with enhanced durability. (2) The PDA carbon coating, characterized by high coating efficiency and PEI-copolymerized crosslink structures, acts as a protective barrier against parasitic electrolyte decomposition. This stabilized the SEI layer and enhanced the electronic conductivity of Si through graphitic conductive channels. (3) The yolk shell structure, achieved by removing the SiO<sub>2</sub> template, created void spaces that effectively accommodated internal mechanical stress resulting from volume-induced fluctuations. (4) The PVP K30 surface protection not only shielded against harsh NaOH etching, preventing structural damage and crack formation in carbon structures, but also imparted flexibility and increased electronic conductivity to rigid, amorphous SiO<sub>2</sub> templates. (5) The proposed hydrothermal route to composite fabrication offers multiple advantages, including increased SiO<sub>2</sub> durability, enhanced PVP K30 loading, and improved carbon coating and crosslinking efficiency.

The thermally stable electrode exhibits satisfactory cycle stability and rate performance, even at temperatures surpassing 700 °C, making it a valuable reference for advancing rattle-type C@void@Si anode materials for high-performance EV applications.

**Supplementary Materials:** The following supporting information can be downloaded at: <https://www.mdpi.com/article/10.3390/batteries10020053/s1>, Figure S1: FE-SEM image of (a) pure Si nanoparticles. (b) FT-IR result comparing pure Si nanoparticles and Si-OH after piranha solution pretreatment; Figure S2: (a) Formation of siloxane networks from piranha-treated Si-OH using APTES.

(b) Hydrolysis and (c) condensation reaction mechanism of TEOS showing formation of siloxane bridges; Figure S3: XPS survey scan of TEOS-SiO<sub>2</sub>@Si and APTES/TEOS-SiO<sub>2</sub>@Si precursors; Figure S4: XRD patterns of (a) Si and (b) TEOS-derived SiO<sub>2</sub>@Si and APTES/TEOS-derived SiO<sub>2</sub>@Si; Figure S5: XRD reference peaks for face-centered cubic Si crystal (Reference code 98-065-2265); Figure S6: TEM images showing carbon crosslinking from PEI and PDA carbon coating efficiency in (a,b) composite samples prepared via traditional SiO<sub>2</sub> sol-gel synthesis reaction and carbon coating at room temperature and (c,d) composite samples prepared via hydrothermal treatment at 140 °C for 24 h; Figure S7: XPS survey spectra of PVP-SiO<sub>2</sub>@Si and Si nanoparticles; Figure S8: XPS survey spectra core shell PDA-PEI@SiO<sub>2</sub>@Si and yolk shell PDA-PEI@SiO<sub>2</sub>@Si composite samples; Figure S9: Illustration of the two possible reaction mechanisms showing the formation of PDA-PEI carbon crosslinks; Figure S10: XPS survey spectra core shell PDA@SiO<sub>2</sub>@Si and yolk shell PDA-PEI@PVP-SiO<sub>2</sub>@Si composite samples; Figure S11: Raman peak fitting of core shell PDA@SiO<sub>2</sub>@Si composite sample; Figure S12: Raman peak fitting of yolk shell PDA-PEI@SiO<sub>2</sub>@Si composite sample; Figure S13: Raman peak fitting of yolk shell PDA-PEI@PVP-SiO<sub>2</sub>@Si composite sample; Figure S14: Raman peak fitting of core shell PDA-PEI@SiO<sub>2</sub>@Si composite sample; Figure S15: CV scans of core shell PDA-PEI@TEOS-SiO<sub>2</sub>@Si composite fabricated via RT using TEOS as precursor solution; Figure S16: Galvanostatic charge and discharge profiles of core shell PDA@SiO<sub>2</sub>@Si (a), core shell PDA-PEI@SiO<sub>2</sub>@Si (b), core shell PDA-PEI@PVP-SiO<sub>2</sub>@Si (c), and yolk shell PDA-PEI@SiO<sub>2</sub>@Si (d) composite samples; Figure S17. Representative SEM images showing the surface morphology of particles in (a,b) yolk shell PDA-PEI@PVP-SiO<sub>2</sub>@Si, (c,d) yolk shell PDA-PEI@SiO<sub>2</sub>@Si, (e,f) core shell PDA-PEI@PVP-SiO<sub>2</sub>@Si, (g,h) core shell PDA-PEI@SiO<sub>2</sub>@Si, and (i,j) core shell PDA@SiO<sub>2</sub>@Si anode (a,c,e,g,i) before and (b,d,f,h,j) after 200 lithiation/delithiation cycles at 1 A g<sup>-1</sup> current density; Table S1: The I<sub>D</sub>/I<sub>G</sub> values of the samples calculated by the ratio of the D band peak area to the G band peak area using Gaussian-Lorentzian curve fitting model; Table S2. The porous structure of the representative composite samples described by BJH model of BET analysis.

**Author Contributions:** Conceptualization, methodology, data curation and visualization, writing—original draft preparation, A.M.; Electrochemical measurements in Figures 14–17, J.J. and H.L.; Resources, H.-H.P.; Funding acquisition, writing—review and editing, submission of manuscript, C.-S.L. All authors have read and agreed to the published version of the manuscript.

**Funding:** This research was funded by a grant funded by the Korea Evaluation Institute of Industrial Technology (grant number: 20220488).

**Data Availability Statement:** The datasets generated and analyzed during the current study are available in Supplementary Materials.

**Conflicts of Interest:** The authors declare no conflicts of interest. The funders had no role in the design of the study; the collection, analyses, or interpretation of data; the writing of the manuscript; or the decision to publish the results.

## References

1. Turner, W.R.; Bradley, B.A.; Estes, L.D.; Hole, D.G.; Oppenheimer, M.; Wilcove, D.S. Climate change: Helping nature survive the human response. *Conserv. Lett.* **2010**, *3*, 304–312. [CrossRef]
2. United Nations (UN). *Paris Agreement*; UN: Geneva, Switzerland, 2015. Available online: [https://unfccc.int/files/essential\\_background/convention/application/pdf/english\\_paris\\_agreement.pdf](https://unfccc.int/files/essential_background/convention/application/pdf/english_paris_agreement.pdf) (accessed on 31 October 2023).
3. United Nations (UN). *United Nations Secretariat Climate Action Plan 2020–2030*; UN: Geneva, Switzerland, 2019. Available online: <https://www.un.org/management/sites/www.un.org.management/files/united-nations-secretariat-climate-action-plan.pdf> (accessed on 1 November 2023).
4. European Union (EU). *2050 Long-Term Strategy*; EU: Brussels, Belgium, 2021. Available online: [https://ec.europa.eu/clima/policies/strategies/2050\\_en](https://ec.europa.eu/clima/policies/strategies/2050_en) (accessed on 1 November 2023).
5. International Energy Agency (IEA). *World Energy Outlook 2022*. 2022. Available online: <https://iea.blob.core.windows.net/assets/830fe099-5530-48f2-a7c1-11f35d510983/WorldEnergyOutlook2022.pdf> (accessed on 1 November 2023).
6. Liang, Y.; Kleijn, R.; Van der Voet, E. Increase in demand for critical materials under IEA Net-Zero emission by 2050 scenario. *Appl. Energy* **2023**, *346*, 121400. [CrossRef]
7. Warner, J.T. *The Handbook of Lithium-Ion Battery Pack Design: Chemistry, Components, Types and Terminology*; Elsevier: Amsterdam, The Netherlands, 2015; pp. 76–79.
8. Pistoia, G. *Lithium-Ion Batteries: Advances and Applications*; Elsevier: Amsterdam, The Netherlands, 2014; pp. 437–438.
9. Fasahat, M.; Manthouri, M. State of charge estimation of lithium-ion batteries using hybrid autoencoder and Long Short Term Memory neural networks. *J. Power Sources* **2020**, *469*, 228375. [CrossRef]

10. Wu, F.; Yushin, G. Conversion cathodes for rechargeable lithium and lithium-ion batteries. *Energy Environ. Sci.* **2017**, *10*, 435–459. [[CrossRef](#)]
11. Weiss, M.; Ruess, R.; Kasnatscheew, J.; Levartovsky, Y.; Levy, N.R.; Minnmann, P.; Stolz, L.; Waldmann, T.; Wohlfahrt-Mehrens, M.; Aurbach, D.; et al. Fast charging of lithium-ion batteries: A review of materials aspects. *Adv. Energy Mater.* **2021**, *11*, 2101126. [[CrossRef](#)]
12. Yang, C. Running battery electric vehicles with extended range: Coupling cost and energy analysis. *Appl. Energy* **2022**, *306*, 118116. [[CrossRef](#)]
13. Wu, F.; Maier, J.; Yu, Y. Guidelines and trends for next-generation rechargeable lithium and lithium-ion batteries. *Chem. Soc. Rev.* **2020**, *49*, 1569–1614. [[CrossRef](#)]
14. Zhang, X.; Li, Z.; Luo, L.; Fan, Y.; Du, Z. A review on thermal management of lithium-ion batteries for electric vehicles. *Energy* **2022**, *238*, 121652. [[CrossRef](#)]
15. Maranchi, J.P.; Hepp, A.F.; Kumta, P.N. High capacity, reversible silicon thin-film anodes for lithium-ion batteries. *ESL* **2003**, *6*, A198. [[CrossRef](#)]
16. Hatchard, T.D.; Dahn, J.R. In situ XRD and electrochemical study of the reaction of lithium with amorphous silicon. *J. Electrochem. Soc.* **2004**, *151*, A838. [[CrossRef](#)]
17. Zhang, W.J. A review of the electrochemical performance of alloy anodes for lithium-ion batteries. *J. Power Sources* **2011**, *196*, 13–24. [[CrossRef](#)]
18. Turcheniuk, K.; Bondarev, D.; Amatucci, G.G.; Yushin, G. Battery materials for low-cost electric transportation. *Mater. Today* **2021**, *42*, 57–72. [[CrossRef](#)]
19. United States Geological Survey (USGS). Mineral Commodity Summaries 2023. 2023. Available online: <https://minerals.usgs.gov/minerals/1030pubs/mcs/2018/mcs2018.pdf> (accessed on 2 November 2023).
20. Cao, Z.; Zheng, X.; Zhou, M.; Zhao, T.; Lv, L.; Li, Y.; Wang, Z.; Luo, W.; Zheng, H. Electrolyte Solvation Engineering toward High-Rate and Low-Temperature Silicon-Based Batteries. *ACS Energy Lett.* **2022**, *7*, 3581–3592. [[CrossRef](#)]
21. Ryu, J.H.; Kim, J.W.; Sung, Y.E.; Oh, S.M. Failure modes of silicon powder negative electrode in lithium secondary batteries. *ESL* **2004**, *7*, A306. [[CrossRef](#)]
22. Wu, B.; Chen, C.; Danilov, D.L.; Jiang, M.; Rajmakers, L.H.J.; Eichel, R.-A.; Notten, P.H.L. Influence of the SEI formation on the stability and lithium diffusion in Si electrodes. *ACS Omega* **2022**, *7*, 32740–32748. [[CrossRef](#)]
23. Shin, J.; Kim, T.H.; Lee, Y.; Cho, E. Key functional groups defining the formation of Si anode solid-electrolyte interphase towards high energy density Li-ion batteries. *Energy Stor. Mater.* **2020**, *25*, 764–781. [[CrossRef](#)]
24. Yang, Y.; Yuan, W.; Kang, W.; Ye, Y.; Yuan, Y.; Qiu, Z.; Wang, C.; Zhang, X.; Ke, Y.; Tang, Y. Silicon-nanoparticle-based composites for advanced lithium-ion battery anodes. *Nanoscale* **2020**, *12*, 7461–7484. [[CrossRef](#)] [[PubMed](#)]
25. Fan, S.; Wang, H.; Qian, J.; Cao, Y.; Yang, H.; Ai, X.; Zhong, F. Covalently bonded silicon/carbon nanocomposites as cycle-stable anodes for Li-ion batteries. *ACS Appl. Mater. Interfaces* **2020**, *12*, 16411–16416. [[CrossRef](#)]
26. Chan, C.K.; Peng, H.; Liu, G.; McIlwrath, K.; Zhang, X.F.; Huggins, R.A.; Cui, Y. High-performance lithium battery anodes using silicon nanowires. *Nat. Nanotechnol.* **2008**, *3*, 31–35. [[CrossRef](#)]
27. Wu, H.; Chan, G.; Choi, J.W.; Yao, Y.; McDowell, M.T.; Lee, S.W.; Jackson, A.; Yang, Y.; Hu, L.; Cui, Y. Stable cycling of double-walled silicon nanotube battery anodes through solid–electrolyte interphase control. *Nat. Nanotechnol.* **2012**, *7*, 310–315. [[CrossRef](#)]
28. Yao, Y.; McDowell, M.T.; Ryu, I.; Wu, H.; Liu, N.; Hu, L.; Nix, W.D.; Cui, Y. Interconnected silicon hollow nanospheres for lithium-ion battery anodes with long cycle life. *Nano Lett.* **2011**, *11*, 2949–2954. [[CrossRef](#)] [[PubMed](#)]
29. Wada, T.; Ichitsubo, T.; Yubuta, K.; Segawa, H.; Yoshida, H.; Kato, H. Bulk-nanoporous-silicon negative electrode with extremely high cyclability for lithium-ion batteries prepared using a top-down process. *Nano Lett.* **2014**, *14*, 4505–4510. [[CrossRef](#)] [[PubMed](#)]
30. Goldman, J.L.; Long, B.R.; Gewirth, A.A.; Nuzzo, R.G. Strain anisotropies and Self-Limiting capacities in Single-Crystalline 3D silicon microstructures: Models for high energy density Lithium-Ion battery anodes. *Adv. Funct. Mater.* **2011**, *21*, 2412–2422. [[CrossRef](#)]
31. Cong, R.; Jo, M.; Martino, A.; Park, H.H.; Lee, H.; Lee, C.S. Three-dimensional network of nitrogen-doped carbon matrix-encapsulated Si nanoparticles/carbon nanofibers hybrids for lithium-ion battery anodes with excellent capability. *Sci. Rep.* **2022**, *12*, 16002. [[CrossRef](#)]
32. Choi, J.Y.; Cong, R.; Martino, A.; Jeon, J.; Lee, H.; Park, J.; Park, H.H.; Lee, C.S. Characteristics and electrochemical performances of nickel@ nano-silicon/carbon nanofibers composites as anode materials for lithium secondary batteries. *Bull. Korean Chem. Soc.* **2023**, *44*, 852–864. [[CrossRef](#)]
33. Noh, E.; Cong, R.; Choi, J.-Y.; Hyun, Y.; Park, H.-H.; Jo, M.; Lee, H.; Lee, C.-S. Synthesis, properties and electrochemical characteristics of SiNPs/CNT/rGO composite films for the anode material of Li ion batteries. *Appl. Nanosci.* **2022**, *12*, 3207–3218. [[CrossRef](#)]
34. Kwon, S.; Jamal, H.; Choi, J.-Y.; Park, H.-H.; Song, J.; Lee, C.-S. Synthesis and characterization of graphene quantum dot/SiNP/carbon nanomaterial composites. *Appl. Nanosci.* **2022**, *12*, 3219–3228. [[CrossRef](#)]
35. Cong, R.; Choi, J.-Y.; Song, J.-B.; Jo, M.; Lee, H.; Lee, C.-S. Characteristics and electrochemical performances of silicon/carbon nanofiber/graphene composite films as anode materials for binder-free lithium-ion batteries. *Sci. Rep.* **2021**, *11*, 1283. [[CrossRef](#)]

36. Hu, R.; Sun, W.; Chen, Y.; Zeng, M.; Zhu, M. Silicon/graphene based nanocomposite anode: Large-scale production and stable high capacity for lithium ion batteries. *J. Mater. Chem. A* **2014**, *2*, 9118–9125. [[CrossRef](#)]
37. Martino, A.; Cong, R.; Jo, M.; Park, H.-H.; Lee, H.; Lee, C.-S. Characteristics and Electrochemical Performance of Hydroxyl-Functionalized Graphene Quantum Dot-Coated Si Nanoparticles/Reduced Graphene Hybrid Anodes for Advanced Li-Ion Batteries. *J. Nanomater.* **2023**, *2023*, 6353894. [[CrossRef](#)]
38. Ramos, A.; Cameán, I.; García, A.B. Graphitization thermal treatment of carbon nanofibers. *Carbon* **2013**, *59*, 2–32. [[CrossRef](#)]
39. Whitener Jr, K.E.; Sheehan, P.E. Graphene synthesis. *Diam. Relat. Mater.* **2014**, *46*, 25–34. [[CrossRef](#)]
40. Landi, B.J.; Ganter, M.J.; Cress, C.D.; DiLeo, R.A.; Raffaele, R.P. Carbon nanotubes for lithium ion batteries. *Energy Environ. Sci.* **2009**, *2*, 638–654. [[CrossRef](#)]
41. Lee, J.; Kim, K.; Park, W.I.; Kim, B.-H.; Park, J.H.; Kim, T.-H.; Bong, S.; Kim, C.-H.; Chae, G.; Jun, M.; et al. Uniform graphene quantum dots patterned from self-assembled silica nanodots. *Nano Lett.* **2012**, *12*, 6078–6083. [[CrossRef](#)]
42. Liu, R.; Wu, D.; Feng, X.; Müllen, K. Bottom-up fabrication of photoluminescent graphene quantum dots with uniform morphology. *J. Am. Chem. Soc.* **2011**, *133*, 15221–15223. [[CrossRef](#)] [[PubMed](#)]
43. Yan, X.; Cui, X.; Li, L.S. Synthesis of large, stable colloidal graphene quantum dots with tunable size. *J. Am. Chem. Soc.* **2010**, *132*, 5944–5945. [[CrossRef](#)] [[PubMed](#)]
44. Yang, L.Y.; Li, H.Z.; Liu, J.; Sun, Z.Q.; Tang, S.S.; Lei, M. Dual yolk-shell structure of carbon and silica-coated silicon for high-performance lithium-ion batteries. *Sci. Rep.* **2015**, *5*, 10908. [[CrossRef](#)]
45. Liu, N.; Wu, H.; McDowell, M.T.; Yao, Y.; Wang, C.; Cui, Y. A yolk-shell design for stabilized and scalable Li-ion battery alloy anodes. *Nano Lett.* **2012**, *12*, 3315–3321. [[CrossRef](#)] [[PubMed](#)]
46. Liu, Z.; Han, S.; Xu, C.; Luo, Y.; Peng, N.; Qin, C.; Zhou, M.; Wang, W.; Chen, L.; Okada, S. In situ crosslinked PVA–PEI polymer binder for long-cycle silicon anodes in Li-ion batteries. *RSC Adv.* **2016**, *6*, 68371–68378. [[CrossRef](#)]
47. Li, C.-G.; Yang, Q.; Chen, D.; Zhu, H.; Chen, J.; Liu, R.; Dang, Q.; Wang, X. Polyethyleneimine-assisted co-deposition of polydopamine coating with enhanced stability and efficient secondary modification. *RSC Adv.* **2022**, *12*, 35051–35063. [[CrossRef](#)]
48. Stöber, W.; Fink, A.; Bohn, E. Controlled growth of monodisperse silica spheres in the micron size range. *J. Colloid Interface Sci.* **1968**, *26*, 62–69. [[CrossRef](#)]
49. Li, W.; Zhao, D. Extension of the Stöber method to construct mesoporous SiO<sub>2</sub> and TiO<sub>2</sub> shells for uniform multifunctional core–shell structures. *Adv. Mater.* **2013**, *25*, 142–149. [[CrossRef](#)]
50. Mogab, C.J.; Adams, A.C.; Flamm, D.L. Plasma etching of Si and SiO<sub>2</sub>—The effect of oxygen additions to CF<sub>4</sub> plasmas. *J. Appl. Phys.* **1978**, *49*, 3796–3803. [[CrossRef](#)]
51. Spierings, G.A.C.M. Wet chemical etching of silicate glasses in hydrofluoric acid based solutions. *J. Mater. Sci.* **1993**, *28*, 6261–6273. [[CrossRef](#)]
52. Proksche, H.; Nagorsen, G.; Ross, D. The Influence of NH<sub>4</sub>F on the Etch Rates of Undoped SiO<sub>2</sub> in Buffered Oxide Etch. *J. Electrochem. Soc.* **1992**, *139*, 521. [[CrossRef](#)]
53. Lou, X.W.; Yuan, C.; Archer, L.A. Double-walled SnO<sub>2</sub> nano-cocoons with movable magnetic cores. *Adv. Mater.* **2007**, *19*, 3328–3332. [[CrossRef](#)]
54. Bühler, J.; Steiner, F.P.; Baltes, H. Silicon dioxide sacrificial layer etching in surface micromachining. *JMM* **1997**, *7*, R1. [[CrossRef](#)]
55. Dai, X.; Liu, H.; Liu, X.; Liu, Z.; Liu, Y.; Cao, Y.; Tao, J.; Shan, Z. Silicon nanoparticles encapsulated in multifunctional crosslinked nano-silica/carbon hybrid matrix as a high-performance anode for Li-ion batteries. *J. Chem. Eng.* **2021**, *418*, 129468. [[CrossRef](#)]
56. Zhang, Q.; Zhang, T.; Ge, J.; Yin, Y. Permeable silica shell through surface-protected etching. *Nano Lett.* **2008**, *8*, 2867–2871. [[CrossRef](#)] [[PubMed](#)]
57. Zhang, Q.; Ge, J.; Goebel, J.; Hu, Y.; Lu, Z.; Yin, Y. Rattle-type silica colloidal particles prepared by a surface-protected etching process. *Nano Res.* **2009**, *2*, 583–591. [[CrossRef](#)]
58. Zhang, H.; Xu, H.; Wu, M.; Zhong, Y.; Wang, D.; Jiao, Z. A soft–hard template approach towards hollow mesoporous silica nanoparticles with rough surfaces for controlled drug delivery and protein adsorption. *J. Mater. Chem. B* **2015**, *3*, 6480–6489. [[CrossRef](#)]
59. Rahman, I.A.; Jafarzadeh, M.; Sipaut, C.S. Synthesis of organo-functionalized nanosilica via a co-condensation modification using  $\gamma$ -aminopropyltriethoxysilane (APTES). *Ceram. Int.* **2009**, *35*, 1883–1888. [[CrossRef](#)]
60. Rai, V.R.; Agarwal, S. Mechanism of self-catalytic atomic layer deposition of silicon dioxide using 3-aminopropyl triethoxysilane, water, and ozone. *Chem. Mater.* **2011**, *23*, 2312–2316. [[CrossRef](#)]
61. Post, P.; Wurlitzer, L.; Maus-Friedrichs, W.; Weber, A.P. Characterization and applications of nanoparticles modified in-flight with silica or silica-organic coatings. *Nanomaterials* **2018**, *8*, 530. [[CrossRef](#)]
62. Dos Santos, F.C.; Harb, S.V.; Menu, M.J.; Turq, V.; Pulcinelli, S.H.; Santilli, C.V.; Hammer, P. On the structure of high performance anticorrosive PMMA–siloxane–silica hybrid coatings. *RSC Adv.* **2015**, *5*, 106754–106763. [[CrossRef](#)]
63. Barr, T.L. An XPS study of Si as it occurs in adsorbents, catalysts, and thin films. *Appl. Surf. Sci.* **1983**, *15*, 1–35. [[CrossRef](#)]
64. Yu, Q.; Ge, P.; Liu, Z.; Xu, M.; Yang, W.; Zhou, L.; Zhao, D.; Mai, L. Ultrafine SiO<sub>x</sub>/C nanospheres and their pomegranate-like assemblies for high-performance lithium storage. *J. Mater. Chem. A* **2018**, *6*, 14903–14909. [[CrossRef](#)]
65. Maaz, M.; Elzein, T.; Dragoe, D.; Bejjani, A.; Jarroux, N.; Poulard, C.; Aubry-Barroca, N.; Nsouli, B.; Roger, P. Poly (4-vinylpyridine)-modified silica for efficient oil/water separation. *J. Mater. Sci.* **2019**, *54*, 1184–1196. [[CrossRef](#)]

66. Yamamoto, S.; Bluhm, H.; Andersson, K.; Ketteler, G.; Ogasawara, H.; Salmeron, M.; Nilsson, A. In situ x-ray photoelectron spectroscopy studies of water on metals and oxides at ambient conditions. *J. Phys. Condens.* **2008**, *20*, 184025. [[CrossRef](#)]
67. Lin, J.; Wang, H.; Ren, E.; Song, Q.; Lan, J.; Chen, S.; Yan, B. Stomatocyte-like hollow polydopamine nanoparticles for rapid removal of water-soluble dyes from water. *Chem. Commun.* **2019**, *55*, 8162–8165. [[CrossRef](#)] [[PubMed](#)]
68. Zhang, Y.; Liu, J.-Y.; Ma, S.; Zhang, Y.-J.; Zhao, X.; Zhang, X.-D.; Zhang, Z.-D. Synthesis of PVP-coated ultra-small Fe<sub>3</sub>O<sub>4</sub> nanoparticles as a MRI contrast agent. *J. Mater. Sci. Mater. Med.* **2010**, *21*, 1205–1210. [[CrossRef](#)]
69. Scharf, T.W.; Ott, R.D.; Yang, D.; Barnard, J.A. Structural and tribological characterization of protective amorphous diamond-like carbon and amorphous CN<sub>x</sub> overcoats for next generation hard disks. *J. Appl. Phys.* **1999**, *85*, 3142–3154. [[CrossRef](#)]
70. Yang, H.-C.; Liao, K.-J.; Huang, H.; Wu, Q.-Y.; Wan, L.-S.; Xu, Z.-K. Mussel-inspired modification of a polymer membrane for ultra-high water permeability and oil-in-water emulsion separation. *J. Mater. Chem. A* **2014**, *2*, 10225–10230. [[CrossRef](#)]
71. Tuinstra, F.; Koenig, J.L. Raman spectrum of graphite. *J. Chem. Phys.* **1970**, *53*, 1126–1130. [[CrossRef](#)]
72. Lee, Y.J. The second order Raman spectroscopy in carbon crystallinity. *J. Nucl. Mater.* **2004**, *325*, 174–179. [[CrossRef](#)]
73. Yuan, X.; Mayanovic, R.A. An empirical study on Raman peak fitting and its application to Raman quantitative research. *Appl. Spectrosc.* **2017**, *71*, 2325–2338. [[CrossRef](#)] [[PubMed](#)]
74. Alvarez Barragan, A.; Nava, G.; Wagner, N.J.; Mangolini, L. Silicon-carbon composites for lithium-ion batteries: A comparative study of different carbon deposition approaches. *J. Vac. Sci. Technol. B* **2018**, *36*, 011402. [[CrossRef](#)]
75. Waseem, M.; Mustafa, S.; Naeem, A.; Shah, K.; Shah, I. Mechanism of Cd (II) sorption on silica synthesized by sol–gel method. *J. Chem. Eng.* **2011**, *169*, 78–83. [[CrossRef](#)]

**Disclaimer/Publisher’s Note:** The statements, opinions and data contained in all publications are solely those of the individual author(s) and contributor(s) and not of MDPI and/or the editor(s). MDPI and/or the editor(s) disclaim responsibility for any injury to people or property resulting from any ideas, methods, instructions or products referred to in the content.